Astronomy & Astrophysics

VERTICO

III. The Kennicutt-Schmidt relation in Virgo cluster galaxies[*]

María J. Jiménez-Donaire[1,2] , Toby Brown[3], Christine D. Wilson[4], Ian D. Roberts[5], Nikki Zabel[6], Sara L. Ellison[7],
Mallory Thorp[7], Vicente Villanueva[8], Ryan Chown[9,10], Dhruv Bisaria[11], Alberto D. Bolatto[8], Alessandro Boselli[12],
Barbara Catinella[13,14], Aeree Chung[15], Luca Cortese[13,14], Timothy A. Davis[16], Claudia D. P. Lagos[13,14],
Bumhyun Lee[17], Laura C. Parker[4], Kristine Spekkens[18], Adam R. H. Stevens[13], and Jiayi Sun[4,19]

(Affiliations can be found after the references)

ABSTRACT

Aims. In this Virgo Environment Traced in CO (VERTICO) science paper, we aim to study how the star formation process depends on the galactic environment and gravitational interactions in the context of galaxy evolution. We explore the scaling relation between the star formation rate surface density (Σ_{SFR}) and the molecular gas surface density (Σ_{mol}), also known as the Kennicutt-Schmidt relation, in a subsample of Virgo cluster spiral galaxies.

Methods. We used new Atacama Compact Array and Total Power (ACA+TP) observations from the VERTICO-Atacama Large Millimeter/submillimeter Array (ALMA) Large Program at 720 pc resolution to resolve the molecular gas content, as traced by the $^{12}CO\,(2-1)$ transition, across the disks of 37 spiral galaxies in the Virgo cluster. In combination with archival UV and IR observations used to determine the star formation rate (SFR), we estimated the parameters of the Kennicutt-Schmidt (KS) relation for the entire ensemble of galaxies, and within individual galaxies.

Results. We find the KS slope for the entire population to be $N = 0.97 \pm 0.07$, with a characteristic molecular gas depletion time of 1.86 Gyr for our full sample, which is in agreement with previous work in isolated, nearby star-forming galaxies. In individual galaxies, we find that the KS slope ranges between 0.69 and 1.40, and that typical star formation efficiencies of molecular gas can vary from galaxy to galaxy by a factor of ~4. These galaxy-to-galaxy variations account for ~0.20 dex in scatter in the ensemble KS relation, which is characterized by a 0.42 dex scatter. In addition, we find that the HI-deficient galaxies in the Virgo cluster show a steeper resolved KS relation and lower molecular gas efficiencies than HI-normal cluster galaxies.

Conclusions. While the molecular gas content in galaxies residing in the Virgo cluster appears – to first order – to behave similarly to that in isolated galaxies, our VERTICO sample of galaxies shows that cluster environments play a key role in regulating star formation. The environmental mechanisms affecting the HI galaxy content also have a direct impact on the star formation efficiency of molecular gas in cluster galaxies, leading to longer depletion times in HI-deficient members.

Key words. galaxies: ISM – galaxies: star formation – galaxies: general

1. Introduction

In the context of galaxy evolution, a key goal of any star formation theory is to understand how efficiently galaxies can convert their interstellar gas content into stars. A common approach to tackle this question is to quantitatively measure the relationship between the gas density and star formation rate (SFR). As such, scaling relations constitute a fundamental tool to investigate star formation, since they arise as a natural consequence of the interplay between physics in star-forming regions and galactic scales. Following Schmidt (1959), who proposed that the rate of star formation is proportional to the square of the gas column density, the work developed by Kennicutt (1989, 1998) on integrated galaxies supported this idea. The well-known Kennicutt-Schmidt (KS) relation connects the SFR and gas surface densities as follows:

$$\Sigma_{SFR} \propto \Sigma_{gas}^{N}, \qquad (1)$$

where N is the power-law index and $\Sigma_{gas} = \Sigma_{HI} + \Sigma_{H_2}$ is the total gas column density, combining the contribution of the atomic

(Σ_{HI}) and molecular (Σ_{H_2}) gas. While Kennicutt (1989, 1998) found $N = 1.40 \pm 0.15$, similar studies employing a range of SFR tracers and varied sampling methodologies derived $N = 0.9–2.1$ (e.g., Buat 1992; Wong & Blitz 2002; Schuster et al. 2007; Kennicutt 2007). Scaling relations, such as the KS relation, depend on both the local physical conditions within the gas and the physics of the galaxy's star-forming disk (e.g., Kennicutt 1998; Wong & Blitz 2002). Therefore, characterizing these relations and their physical scatter has the potential to provide unique insight into the physics and scales that regulate star formation.

Intuitively, however, the connection between Σ_{SFR} and Σ_{H_2} is physically more appropriate, since star formation takes place within cold molecular gas. While this process takes places locally, inside molecular clouds, it is extremely complex to characterize since it involves physical mechanisms that affect a wide range of physical scales (from star-forming clumps to giant molecular cloud complexes) and densities (~$10^2–10^6$ cm^{-3}). Tracing the total molecular component of the gas is key to understand star formation in detail (e.g., McKee & Ostriker 2007; Lada et al. 2010, 2012; Longmore et al. 2013; Klessen & Glover 2016); however, H$_2$ molecules are very difficult to observe directly. The main reason for this is that the H$_2$ molecule lacks a dipole moment, as well as the low temperatures found in molecular

---

[*] FITS files for the figures are only available at the CDS via anonymous ftp to `cdsarc.cds.unistra.fr` (`130.79.128.5`) or via `https://cdsarc.cds.unistra.fr/viz-bin/cat/J/A+A/671/A3`

clouds, which prevents vibrational excitation. Observers usually trace the majority of molecular gas indirectly instead, via the carbon monoxide (CO) rotational transitions. Given its large abundance, CO is the next most reliable molecular tracer in the universe (for an in-depth review, see Bolatto et al. 2013).

Over the last decade, extensive CO mapping across nearby galaxies has been possible thanks to the great sensitivity and speed of single-dish radio telescopes and interferometers. These routine observations have tremendously improved our understanding of the physics regulating star formation in galaxies. High spatial resolution datasets (e.g., 700 pc) have allowed studies such as the seminal work by Bigiel et al. (2008) to show that a KS-type power law with an index $N = 1.0 \pm 0.2$ holds down to subkiloparsec scales between Σ_{SFR} and Σ_{H2} across a large sample of spiral, star-forming galaxies. Later studies have also found $N \sim 0.8-1.4$ for this KS relation (e.g., Blanc et al. 2009; Schruba et al. 2011; Leroy et al. 2013; Usero et al. 2015; Lin et al. 2019; Ellison et al. 2021a; Pessa et al. 2021) , and reinforced that Σ_{SFR} is strongly correlated with the local Σ_{H_2}, and only tangentially connected to the atomic gas content.

While the power-law index N can strongly depend on the methods used to quantify gas masses and SFRs, the variation in the scatter has also been related to distinct evolutionary life cycles in individual star-forming regions (e.g., Schruba et al. 2010). In addition, there is growing evidence that the galactic environment can potentially regulate the molecular gas and its connection to star formation. Within galaxies, it has been shown that galactic structures and galactic environment can alter the molecular gas probability distribution functions and the evolution of giant molecular clouds (e.g., Hughes et al. 2013; Colombo et al. 2014; Sun et al. 2020, 2022; Meidt et al. 2021). The giant molecular cloud mass distribution function is steeper in the inter-arm region than in the spiral arms; also, more massive clouds, characterized by larger turbulence, tend to reside in environments at higher gas, star, and SFR surface densities, and stronger shear. Even at larger scales, the molecular efficiency of star formation has been shown to be directly affected in cluster environments due to enhanced H_2 masses as well as triggered star formation when compared to their field counterparts (e.g., Mok et al. 2017). These differences could in turn be reflected in changes in the KS slope and scatter, which are directly related to a variation in molecular gas densities and star formation properties across the disk of cluster members. The general dependence of the KS parameters on spatial scale is still unclear. While studies such as Williams et al. (2018) found that the molecular KS index strongly decreases with increasing scales, becoming approximately linear at approximately kiloparsec scales, Pessa et al. (2021) recently found no evidence for systematic dependences of the slope on the spatial resolution of the Physics at High Angular resolution in Nearby GalaxieS (PHANGS) data.

This KS star formation relation was initially studied in spiral, isolated galaxies. Later studies, however, showed that the KS relation also applies in samples of unresolved cluster spiral galaxies (Fumagalli & Gavazzi 2008; Vollmer et al. 2012). However, it is still unclear whether the KS relation is affected by the environment in which galaxies reside (e.g., Boquien et al. 2011; Lizée et al. 2021; Vollmer et al. 2021). There is plenty of evidence that the SFR of galaxies in clusters is significantly reduced (see e.g., Boselli et al. 2022, and references therein), which could, in turn, modify the expected KS relation. The surrounding environment, indeed, might perturb the relation between gas column density and SFR both at galactic scales or within galactic disks. The large variation found for the power-

law indices and the scatter at fixed molecular gas surface densities makes it unclear whether a unique star formation law could hold among and within galaxies. Several Virgo cluster galaxies that are affected by ram pressure stripping have been studied by Nehlig et al. (2016) and Lee et al. (2017), finding no significant variations from the global KS relation from Kennicutt (1998). Nevertheless, these galaxies showed clear regions with varying depletion times where the gas is compressed due to ram pressure stripping, in the sense that the SFRs are higher in regions where the intracluster medium exerts a higher pressure.

Resolving galaxy disks inside cluster environments constitutes a unique laboratory to study star formation. These gravitationally bound environments can evolve in a different way than their galaxy counterparts in the field. Their diverse and often extreme environments, as well as interactions between members, could have a great impact on their molecular gas content (Violino et al. 2018; Pan et al. 2018; Thorp et al. 2022), which may affect the star formation rates in a variety of fashions. In recent years, observations have shown that physical processes within galaxy clusters, such as ram-pressure stripping (e.g., Gunn et al. 1972; Cortese et al. 2021) or galaxy-to-galaxy interactions such as harassment or mergers, have a great impact on their atomic gas content (Boselli & Gavazzi 2006, 2014). In addition, these interactions have been shown to clearly affect the molecular gas content in the cluster members, as evidenced by the galaxy members in the Virgo cluster (Fumagalli et al. 2009; Boselli et al. 2014). Given that molecular gas constitutes the immediate fuel for star formation, the cluster galaxies' environment is directly shaped, both morphologically and kinematically, by their members' interactions (e.g., Lee et al. 2017; Lee & Chung 2018; Zabel et al. 2019; Lizée et al. 2021). Understanding how cluster environments are connected to the local-scale star formation rates and molecular gas, star formation efficiency is therefore key to constrain theories of star formation and galaxy evolution (Chung & Kim 2014; Nehlig et al. 2016; Moretti et al. 2020; Cramer et al. 2020, 2021; Lee et al. 2020; Boselli et al. 2022).

Investigating whether there are significant differences in the KS law between star-forming regions in cluster galaxies and those of normal, star-forming disks is key to understand the imprint of cluster environments on the star formation process at subkiloparsec scales. To address these questions, we employed a wide set of multiwavelength data to trace star formation and molecular gas, and we measured Σ_{SFR} and Σ_{H2} in a sample of 37 galaxies from the Virgo cluster of galaxies. The present study constitutes one of the first science papers from the Virgo Environment Traced in CO (VERTICO, Brown et al. 2021) program. While recent efforts have been made in this direction, VERTICO is the first survey probing the molecular gas content at subkiloparsec scales in a complete and statistically significant number of galaxies of the Virgo cluster. By measuring CO in a homogeneous fashion, over a wide variety of regions, VERTICO is ideal for revealing the dependencies of local star formation efficiency (SFE) with gas density and location as a function of environmental influence for the first time. By analyzing the KS relation in cluster members, this study is in a unique position to unravel the mechanisms that regulate star formation at subkiloparsec scales inside a galaxy cluster environment.

This paper is organized as follows: in Sect. 2 we describe the VERTICO observations and data reduction, while Sect. 3.1 provides an overview of the ancillary data used to complement the VERTICO dataset. In Sect. 4 we detail the main methods to convert the observable quantities into the main physical parameters. We present our main results in Sect. 5 and provide a discussion and an interpretation in Sect. 6. Finally a short summary of our work can be found in Sect. 7.

Table 1. VERTICO subsample of low-inclination ($i \leq 80°$) galaxies.

Galaxy	RA (hh:mm:ss)	Dec (dd:mm:ss)	i (°)	PA (°)	$\log_{10}$ SFR ($M_\odot\,\mathrm{yr}^{-1}$)	$\log_{10} M_*$ ($M_\odot$)	$\mathrm{def}_{\mathrm{HI}\,M_*}$ (dex)
IC3392	12:28:43	+14:59:57	68	219	−1.30	9.51	$1.50^{+0.02}_{-0.02}$
NGC4064	12:04:11	+18:26:39	70	150	−1.07	9.47	$1.50^{+0.01}_{-0.02}$
NGC4189	12:13:47	+13:25:35	42	70	−0.33	9.75	$0.63^{+0.07}_{-0.03}$
NGC4254	12:18:50	+14:25:06	39	243	0.70	10.52	$-0.03^{+0.02}_{-0.06}$
NGC4293	12:21:13	+18:23:03	67	239	−0.27	10.50	$2.16^{+0.02}_{-0.09}$
NGC4294	12:21:18	+11:30:39	74	151	−0.39	9.38	$0.18^{+0.02}_{-0.12}$
NGC4298	12:21:33	+14:36:20	52	132	−0.26	10.11	$0.68^{+0.06}_{-0.16}$
NGC4299	12:21:41	+11:30:06	14	128	−0.34	9.06	$-0.72^{+0.53}_{-0.30}$
NGC4321	12:22:55	+15:49:33	32	280	0.54	10.71	$0.36^{+0.03}_{-0.01}$
NGC4351	12:24:01	+12:12:15	48	251	−0.91	9.37	$0.55^{+0.02}_{-0.13}$
NGC4380	12:25:22	+10:01:00	61	158	−0.77	10.11	$1.27^{+0.06}_{-0.16}$
NGC4383	12:25:25	+16:28:12	56	17	0.01	9.44	$-0.39^{+0.01}_{-0.05}$
NGC4394	12:25:56	+18:12:52	32	312	−0.79	10.34	$0.90^{+0.06}_{-0.00}$
NGC4405	12:26:07	+16:10:52	46	18	−0.88	9.75	$1.73^{+0.07}_{-0.03}$
NGC4419	12:26:56	+15:02:51	74	131	−0.12	10.06	$1.65^{+0.11}_{-0.13}$
NGC4424	12:27:12	+09:25:14	61	274	−0.52	9.89	$1.14^{+0.07}_{-0.07}$
NGC4450	12:28:29	+17:05:05	51	170	−0.55	10.70	$1.35^{+0.03}_{-0.00}$
NGC4457	12:28:59	+03:34:14	37	256	−0.49	10.42	$1.29^{+0.06}_{-0.04}$
NGC4501	12:31:59	+14:25:11	65	320	0.43	11.00	$0.80^{+0.03}_{-0.02}$
NGC4532	12:34:19	+06:28:06	64	159	−0.16	9.25	$-0.25^{+0.12}_{-0.05}$
NGC4535	12:34:20	+08:11:54	48	12	0.31	10.49	$0.07^{+0.02}_{-0.10}$
NGC4536	12:34:27	+02:11:16	74	118	0.47	10.19	$-0.26^{+0.02}_{-0.08}$
NGC4548	12:35:27	+14:29:44	37	318	−0.28	10.65	$0.96^{+0.02}_{-0.02}$
NGC4561	12:36:08	+19:19:22	28	60	−0.64	9.09	$-0.64^{+0.41}_{-0.46}$
NGC4567	12:36:33	+11:15:29	49	251	0.03	10.25	$-0.27^{+0.00}_{-0.04}$
NGC4568	12:36:34	+11:14:22	70	211	0.29	10.47	$0.40^{+0.01}_{-0.09}$
NGC4569	12:36:50	+13:09:55	69	203	0.16	10.86	$1.12^{+0.03}_{-0.04}$
NGC4579	12:37:43	+11:49:06	40	273	0.08	10.92	$1.20^{+0.02}_{-0.04}$
NGC4580	12:37:48	+05:22:06	46	337	−0.90	9.94	$1.99^{+0.11}_{-0.07}$
NGC4606	12:40:58	+11:54:44	69	38	−1.33	9.61	$1.86^{+0.01}_{-0.02}$
NGC4651	12:43:43	+16:23:38	53	75	−0.10	10.31	$0.09^{+0.03}_{-0.00}$
NGC4654	12:43:57	+13:07:33	61	300	0.31	10.26	$-0.01^{+0.00}_{-0.03}$
NGC4694	12:48:15	+10:59:01	62	323	−0.85	9.94	$1.03^{+0.11}_{-0.07}$
NGC4698	12:48:23	+08:29:15	66	347	−0.83	10.49	$0.37^{+0.02}_{-0.10}$
NGC4713	12:49:58	+05:18:40	45	89	−0.20	9.31	$-0.42^{+0.10}_{-0.00}$
NGC4772	12:53:29	+02:10:06	60	325	−1.08	10.18	$0.48^{+0.02}_{-0.09}$
NGC4808	12:55:49	+04:18:15	72	127	−0.19	9.63	$-0.27^{+0.01}_{-0.03}$

Notes. The right ascension and declination of the galaxies optical centers are taken from the NASA/IPAC Extragalactic Database (https://ned.ipac.caltech.edu/). The orientation parameters (optical inclinations and position angles) are drawn from Brown et al. (2021), and are calculated using fits to SDSS photometry. The average star formation rates and integrated stellar mass are adopted from Leroy et al. (2019). HI deficiencies are adopted from Zabel et al. (2022), and are calculated using the predicted HI mass from field galaxies at fixed stellar mass.

2. Observations and data reduction

We use a subsample of 37 galaxies included in the VERTICO[1] (Brown et al. 2021) survey. The full VERTICO sample consists of a total of 51 Virgo Cluster galaxies, selected from the Very Large Array Imaging of Virgo in Atomic Gas survey (VIVA, Chung et al. 2009) because their environment seems to be actively affecting them, via ram pressure stripping, starvation, and tidal interaction. In addition, these sources cover a wide range of star formation properties and span two orders of magnitude in stellar mass. Our selected subsample only excludes highly inclined ($i > 80°$) targets from the original dataset, in order to minimize any major projection effects. A summary with the basic properties of the working sample of galaxies can be found in Table 1, orientation parameters are drawn from

[1] https://www.verticosurvey.com/

Brown et al. (2021), global SFR and stellar masses are adopted from Leroy et al. (2019), and HI deficiencies are calculated using the predicted HI mass from field galaxies at fixed stellar mass, from Zabel et al. (2022). Based on Mei et al. (2007), we employ a common distance of 16.5 Mpc to all Virgo galaxies throughout the paper.

The observations for VERTICO were carried out using the ALMA Atacama Compact Array (ACA) during Cycle 7 (2019.1.00763.L.). Out of the total 51 galaxies in the sample, 37 targets were newly observed, while 15 galaxies were already surveyed and the data were publicly available in the ALMA archive (Cramer et al. 2020; Leroy et al. 2021). From our selected subsample, 13 galaxies had archival data (NGC 4254, NGC 4321, NGC 4293, NGC 4298, NGC 4424, NGC 4457, NGC 4535, NGC 4536, NGC 4548, NGC 4569, NGC 4579, NGC 4654, NGC 4694). To recover the CO extended emission at large angular scales, Total Power (TP) observations were needed for 25 out of 37 targets. The VERTICO program targeted spectroscopic observations of the ^{12}CO (2–1) transition, as well as the main isotopologues ^{13}CO (2–1) and C^{18}O (2–1) and ALMA Band 6 continuum. For each galaxy, a Nyquist-sampled mosaic was performed in order to map their molecular gas disk. The nominal flux calibration uncertainty of ALMA in Band 6 during Cycle 7 was 5–10% according to the ALMA Cycle 7 Technical Handbook. A detailed description of the data reduction and imaging process is available in Brown et al. (2021).

After imaging, two working datasets were generated by convolving each datacube to 9″ resolution and 15″ resolution, which correspond to physical scales of 720 pc and 1.2 kpc respectively, at the distance of Virgo. While most of our work is carried out using the final products at 9″ resolution, these two resolution sets allow us to beam-match the observations to ancillary infrared data and UV data, needed for the analysis (see Sect. 4). Integrated intensity maps are computed directly from these final data products, implementing a masking process described in Sun et al. (2018). This method employs a spatially and spectrally varying noise, which we measure in every pixel and channel before primary beam correction. For that, a mask is generated by combining a core mask, selecting spaxels with $S/N \geq 3.5$ in three consecutive channels or more, and a wing mask for spaxels with $S/N \geq 2$ in two consecutive channels or more. We refer the reader to the VERTICO survey paper Brown et al. (2021) for a detailed description of the method implementation. Moment-0 maps are then calculated the integrated intensity along the spectral axis in K km s^{-1}. We further convert these line measurements into molecular gas surface densities, as described in Sect. 4.1.

3. Ancillary data and control sample

3.1. Ancillary data

All galaxies in the VERTICO sample are well-studied Virgo galaxies with existing datasets in a wide range of wavelengths, which allows us to characterize and compare the distributions of gas, stars and recent star formation.

We employ a combination of near-UV as well as near- and mid-IR photometry to derive star formation rates and stellar masses, following Leroy et al. (2019). In particular, we use near ultra-violet $\lambda = 231$ nm data (hereafter NUV) from the Galaxy Evolution Explorer (GALEX, Martin et al. 2005). The near and mid-IR data were taken from the Wide-field Infrared Survey Explorer (WISE, Wright et al. 2010), from which we use WISE bands 1 ($\lambda = 3.4$ μm), 3 ($\lambda = 12$ μm) and 4 ($\lambda = 22$ μm).

3.2. Extragalactic CO sample: HERACLES

In this study we make use of the HERA CO-Line Extragalactic Survey (HERACLES, Leroy et al. 2009) to compare the kpc scale properties of the VERTICO targets with a resolved sample of field galaxies. HERACLES is a large program that used the IRAM-30m single-dish telescope to provide wide-field CO(2-1) emission maps of molecular gas sampled at ~13″ resolution, which corresponds to ~500 pc at the median distance of the sample, inside the optical radius of nearby galaxies. The final sample consisted of 48 nearby, star-forming galaxy disks, which have good CO extent and sensitivity well beyond the HI-H$_2$ transition radius. We use a final subsample of 21 HERACLES galaxies detected in CO, after removing galaxy duplicates in both samples (NGC 4254, NGC 4321, NGC 4536, NGC 4569, and NGC 4579) and interacting candidates (NGC 2146, NGC 2798, NGC 3034, NGC 3077, and NGC 5713). The resolved working observables are calculated direcly from the HERACLES data products at native resolution, using the VERTICO pipeline (see Brown et al. 2021, for a detailed description). The HERACLES sample of galaxies is drawn from previous extragalactic surveys that provide data across different wavelengths such as The HI Nearby Galaxy Survey (THINGS, Walter et al. 2008) and the *Spitzer* Infrared Nearby Galaxies Survey (SINGS, Kennicutt 2003). As previously described in Zabel et al. (2022), these samples were constructed with galaxies following an approximately flat far-infrared (FIR) luminosity distribution. As a result, the HERACLES sample under-represents FIR-faint galaxies and it is likely biased toward galaxies with large gas mass by design.

4. Physical parameters

4.1. Molecular gas

The molecular gas mass surface densities can be estimated using the velocity-integrated CO (1–0) observations, as a probe of the molecular gas content. In this paper, we derive the molecular surface densities directly from the VERTICO and HERACLES surveys CO (2–1) integrated intensity maps, assuming a fixed CO(2–1)-to-CO (1–0) line ratio, R_{21}, of 0.7 as derived by Brown et al. (2021). This line ratio value agrees well with previous results for normal star-forming galaxies in the literature, such as HERACLES (0.46−0.97), EMPIRE (0.51−0.87) and PHANGS (0.50−0.83), using both transition lines at matched resolution in nearby, star-forming galaxies (e.g., Leroy et al. 2013, 2022; Jiménez-Donaire et al. 2019; den Brok et al. 2021). We derive the molecular surface density as

$$\Sigma_{\mathrm{mol}} = \alpha_{\mathrm{CO}} \frac{I_{\mathrm{CO}(2-1)}}{R_{21}} \cos(i), \qquad (2)$$

where i is the inclination of the galaxy disk. α_{CO} is the CO-to-molecular mass conversion factor for the CO (1–0) transition. Throughout the paper we assume a constant Galactic value, $\alpha_{\mathrm{CO}}^{\mathrm{MW}} = 4.35\ M_\odot\ \mathrm{pc}^{-2}(\mathrm{K\ km\ s}^{-1})^{-1}$ (see Bolatto et al. 2013, for a detailed description of its derivation), for which the corresponding X_{CO} is $2 \times 10^{20}\ \mathrm{cm}^{-2}(\mathrm{K\ km\ s}^{-1})^{-1}$. We use this value for consistency with previous VERTICO works (Brown et al. 2021; Zabel et al. 2022), as well as other CO nearby galaxy surveys (e.g., Leroy et al. 2009; Wilson et al. 2009; Saintonge et al. 2011; Bolatto et al. 2017, but see Table 2 for an overview). This value already includes a 1.36 factor to account for the presence of helium. It is well known that the CO-to-H$_2$ conversion factor depends on metallicity (Wilson 1995; Boselli et al. 2002; Bolatto et al. 2013; Sandstrom et al. 2013). The galaxies analyzed in this work are all massive spirals with a similar metallicity range. We thus decided to use a similar conversion factor for

Table 2. Literature compilation of slopes from resolved molecular KS relations.

Reference	Index (N)	Scale	α_{CO} ($M_\odot\,pc^{-2}/(K\,km\,s^{-1})$)	Fitting method
VERTICO	0.97 ± 0.07	720 pc	4.35	Least Trimmed Squares
Querejeta et al. (2021)	0.97 ± 0.06 [a]	$\sim 1-2$ kpc	$4.35 \times Z'^{-1.6}$	Bisector Ordinary Least Squares (OLS)
Pessa et al. (2021)	1.06 ± 0.01	100 pc	$4.35 \times Z'^{-1.6}$	OLS
Sánchez et al. (2021)	0.95 ± 0.21	$\sim$kpc	4.3	OLS
Ellison et al. (2021a)	0.86 ± 0.01	$\sim$kpc	4.3	Orthogonal Distance Regression (ODR)
Morselli et al. (2020)	0.80 ± 0.12	500 pc	4.3	OLS
Lin et al. (2019)	1.05 ± 0.01	$\sim$kpc	4.3	ODR
Usero et al. (2015)	1.01 ± 0.08	$\sim 1-2$ kpc	4.4	Total Least Squares
Leroy et al. (2013)	1.00 ± 0.15	$\sim$kpc	4.35	Monte Carlo fitting
Schruba et al. (2011)	1.0 ± 0.1	$\sim 0.2-2$ kpc	4.35	Bisector OLS
Genzel et al. (2010)	1.17 ± 0.09	$>$kpc	4.35 [b]	Not specified
Daddi et al. (2010)	1.31 ± 0.09	$>$kpc	3.6 [c]	Not specified
Blanc et al. (2009)	0.82 ± 0.05	$\sim$750 pc	6.0 [d]	Monte Carlo fitting
Bigiel et al. (2008)	1.0 ± 0.02	$\sim$750 pc	4.35	Bisector OLS
Kennicutt (2007)	1.37 ± 0.03	$\sim$500 pc	6.0 [d]	Bivariate Least Squares

Notes. The α_{CO} factors correspond to the CO (1-0) transition. [a]Querejeta et al. (2021) report a range of values between $0.90-1.43$ for the slopes, which is due to the choice of α_{CO} conversion factor. [b]Genzel et al. (2010) employ a conversion factor of 4.35 for star-forming galaxies (SFGs) and 1.36 for submillimeter galaxies (SMGs). [c]Daddi et al. (2010) use a conversion factor of 3.6 for $z = 0.5-2.5$ normal galaxies, 4.6 for local spirals, and 0.8 for local ULIRGs and distant SMGs. [d]Blanc et al. (2009) and Kennicutt (2007) adopt the conversion factor derived in Bloemen et al. (1986), with $X_{CO} = 2.8 \times 10^{20}\,cm^{-2}\,(K\,km\,s^{-1})^{-1}$.

all of them. Second order effects related to the observed metallicity gradients in galaxies might induce systematic effects in the radial variation of the deduced molecular gas column density. The recent analysis of PHANGS galaxies done by Pessa et al. (2021), however, suggests that these effects, if present, are negligible and thus justify our choice of a constant conversion factor. An example of molecular mass surface density map can be found on the right panel of Fig. 1, for the VERTICO galaxy NGC 4501.

4.2. Star formation rates

Our resolved star formation rate measurements are obtained from GALEX and WISE photometry following the procedure laid out in Leroy et al. (2019). All images are convolved from their native resolution to a common working resolution of 9″, using the Aniano et al. (2011) convolution kernels. All *Gaia* Data Release (DR) 2 stars within the image area were masked. Image backgrounds are estimated and subtracted with the Astropy Background2D function.

Star formation rate maps were constructed from a combination of GALEX NUV and WISE3 photometry. The left panel of Fig. 1 shows an example of SFR map for the VERTICO galaxy NGC 4501. We use WISE3 images to quantify the obscured SFR at an angular resolution of 9″ similar to the one reached by ALMA. The WISE3 band is preferred to the WISE4 band at 22 μm for its better angular resolution, although the latter is believed to be a better SFR tracer due to less contamination from polycyclic aromatic hydrocarbons (PAH) emission (Boselli et al. 2004). That said, Leroy et al. (2019) show that WISE4 is a much more robust SFR tracer than WISE3, despite the higher sensitivity and resolution of WISE3 imaging. To address this we apply a pixel-by-pixel WISE3-to-WISE4 color correction to the WISE3 images. Specifically, for each galaxy we fit a linear relation between WISE3/WISE4 color and galactocentric radius and then modify the WISE3 image on a pixel-by-pixel basis according to the galactocentric radius of each pixel and the expected WISE3/WISE4 ratio from the linear fit. A detailed

derivation of these maps can be found in Roberts et al. (in preparation). This approach is also suggested in the Appendix of Leroy et al. (2019) for cases where it is necessary to use WISE3 over WISE4 as the mid-IR SFR tracer. With GALEX NUV and color-corrected WISE3 images for each galaxy, we then apply the NUV+WISE4 SFR calibration from Leroy et al. (2019) to derive spatially resolved SFR maps in units $M_\odot$/yr/kpc^2. This employs the stellar initial mass function of Kroupa & Weidner (2003) with bounds of 0.1 and 100 $M_\odot$, a slope -2.35 between 1 and 100 $M_\odot$, and a slope of -1.3 between 0.1 and 1 $M_\odot$. The same procedure was followed to construct resolved SFR maps for all of the HERACLES galaxies, therefore ensuring a homogeneous comparison between galaxy samples. We compared our estimated SFRs for the subsample of galaxies that are also included in HERACLES, to the SFRs calculated in Leroy et al. (2013) and Bigiel et al. (2008) using a combination of GALEX FUV and 24 μm images. For that subsample of galaxies, we find that variations are on the order of $\sim$7%.

5. Results

In this section we present our main results for the resolved Kennicutt-Schmidt relation in the VERTICO galaxies, and we explore how this relation changes with angular resolution. We show the resolved relation for the full sample of galaxies included in Table 1 as well as for each individual galaxy to analyze galaxy-to-galaxy variations. In addition, we explore how HI-deficiency may impact the shape of the KS relation and the depletion times observed in the full sample.

5.1. Ensemble star formation relations in VERTICO

Figure 2 shows the relation between the star formation rate surface density, Σ_{SFR}, and the molecular gas surface density, Σ_{mol}, for the ensemble sample of galaxies selected from VERTICO. The left panel shows the VERTICO data at 9″ (720 pc) resolution, while the right panel shows the same dataset convolved to
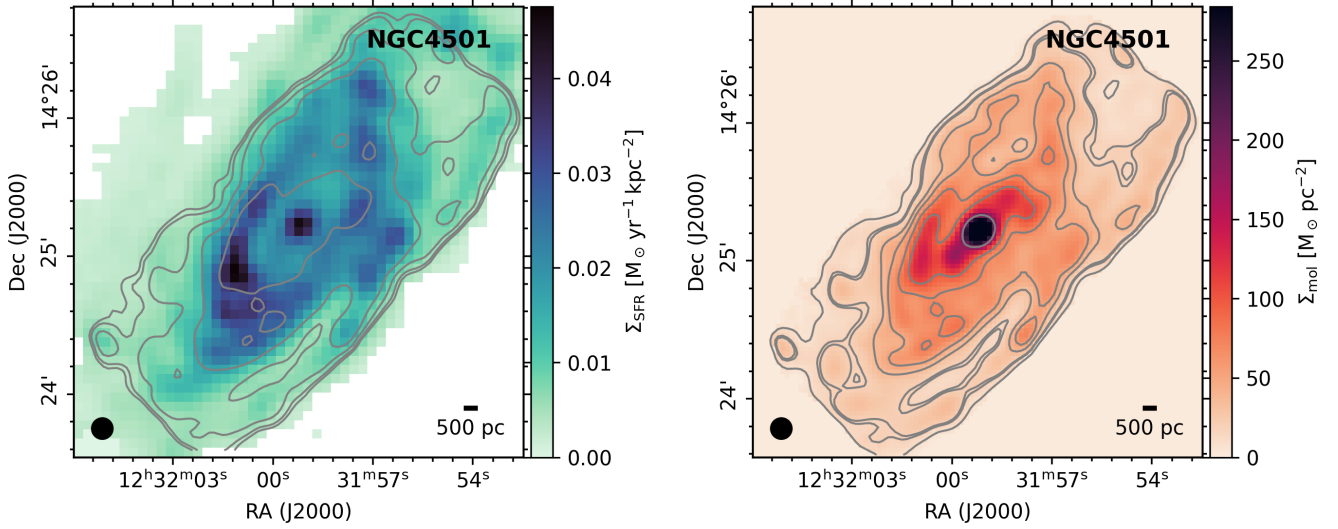
Fig. 1. Example of the data products used for each galaxy in the VERTICO survey. *Left*: SFR surface density measured for NGC 4501 using GALEX NUV and WISE3 photometry. *Right*: Molecular gas surface density map derived from the VERTICO CO (2–1) data products. Molecular gas surface brightness contours at 3, 5, 10, 20 and 40-σ detection are overlaid on both panels. The illustrated beam in the lower left corner of each panel is 9″ in diameter and represents the working angular resolution. This beam corresponds to 720 pc at the distance of Virgo (16.5 Mpc). The complete figure set for the VERTICO subsample used in this paper is available online.
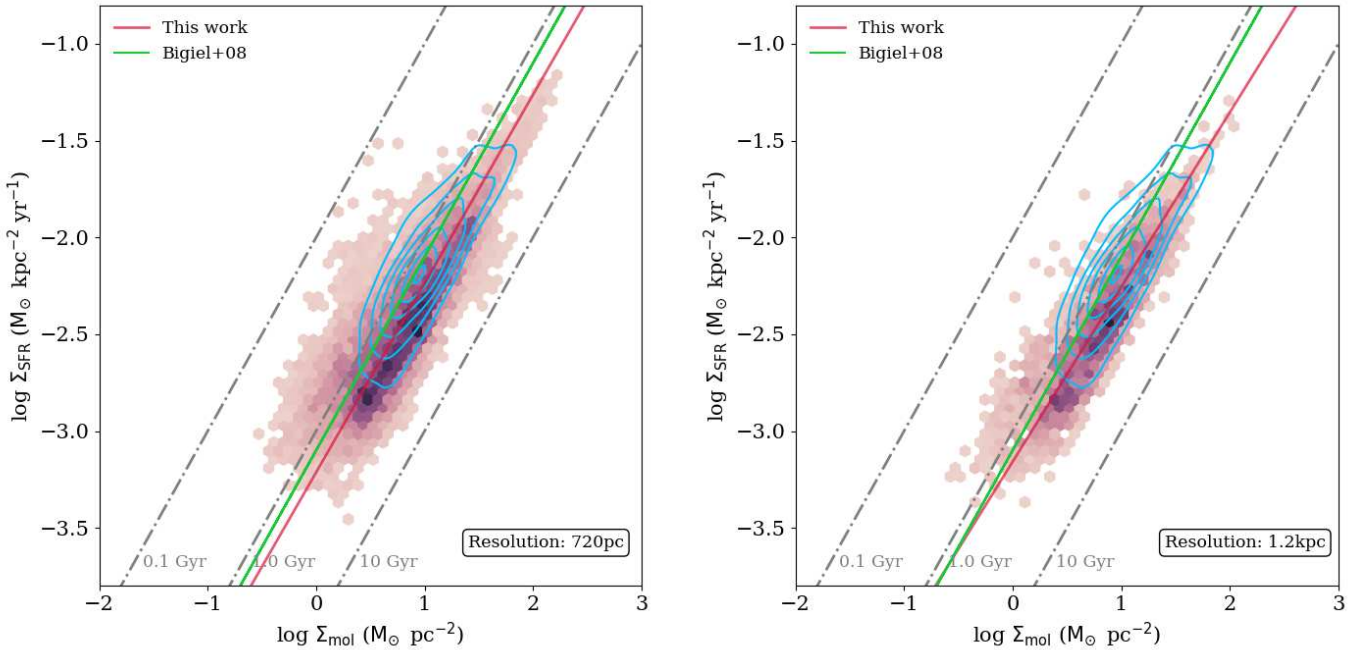
Fig. 2. Resolved KS relation for the ensemble of VERTICO galaxies at a resolution of 720 pc (*left*) and for the data convolved to a linear resolution of 1.2 kpc (*right*). Only galaxies with $i < 80°$ have been selected, excluding edge-on targets, in order to avoid absorption and strong projection effects. Color code shows increasing point density. Contours show the corresponding KS relation using the sub-sample of field galaxies extracted from the HERACLES survey. We note that values for Σ_{SFR} and Σ_{mol} have been corrected to face-on via $\cos i$.

15″, corresponding to physical scales of 1.2 kpc. In both panels, the individual bins are color-coded by point density, where brighter colors show higher density of data points. The panels also include levels of constant depletion times of 0.1, 1.0, and 10 Gyr, respectively, as dashed gray lines. These diagonal lines represent an estimation of the time that the rate of star formation would need in order to deplete the molecular gas reservoir to produce stars.

The blue contours shown on top of the VERTICO data correspond to sub-samples of HERACLES field galaxies, chosen to match the fixed-physical scales samples in each panel.

Therefore, these data are also plotted at 720 pc and 1.2 kpc resolution in order to compare two datasets that are intrinsically very different, between cluster and field galaxies. The plot shows that the KS relation between SFR surface density and the molecular gas surface density for the high-density points of VERTICO galaxies is very similar to that found for the HERACLES field galaxies. The scatter in the data shown in Fig. 2 is approximately symmetric around depletion times of 1–3 Gyr. Figure 2 therefore demonstrates visually the first main conclusion of this paper: when considered as an ensemble, the

Table 3. Best-fit values for the ensemble VERTICO samples.

Sample	Index (N)	$\log_{10} A$ ($\log_{10} M_\odot \, \mathrm{yr}^{-1} \, \mathrm{pc}^2$)	σ (dex)
Galaxies: 720 pc	0.97 ± 0.07	-3.20 ± 0.08	0.42
Galaxies: 1.2 kpc	0.91 ± 0.08	-3.15 ± 0.11	0.35
HI-deficient	0.93 ± 0.04	-2.98 ± 0.09	0.30
HI-normal	0.84 ± 0.04	-3.26 ± 0.10	0.41

Notes. Best-fit slope (N), intercept (referenced to Σ_{mol} units of $1\,M_\odot\,\mathrm{pc}^{-2}$), and scatter ($\sigma$) results for the resolved KS relation in the VERTICO sample, comparing the ensembles at 720 pc and 1.2 kpc resolution, as well as the HI-normal and HI-deficient samples of galaxies.

KS relation for Virgo cluster disk galaxies is consistent with field galaxies.

In order to better quantify this relation, we perform a robust linear regression following the method presented in Cappellari et al. (2013), which implements the least trimmed squares (LTS) regression approach of Rousseeuw (1984). This method takes into account the uncertainties in all variables, the presence of outliers in the data, as well as unknown intrinsic scatter in excess of uncertainties. Expressing the power-law relation $\Sigma_{\mathrm{SFR}} = a\,(\Sigma_{\mathrm{mol}})^N$, in log-space as:

$$\log \Sigma_{\mathrm{SFR}} = A + N \log \Sigma_{\mathrm{mol}}, \tag{3}$$

we can identify N as the slope of the KS relation, and $A = \log_{10} a$ as the intercept. We treat both Σ_{SFR} and Σ_{mol} as independent variables with uncertainties, and quote the fitting results in Table 3. We derive a slope of 0.97 ± 0.07 for the resolved KS relation for the VERTICO data at 720 pc, and an intrinsic scatter about the fit of 0.42 dex.

Since molecular cloud formation, stellar feedback, and the significance of SFR tracers can depend strongly on spatial scales (e.g., Orr et al. 2018; Hani et al. 2020), we investigate whether the resolved KS relation experiences any changes when working at a significantly lower resolution. We perform the same robust fit to the data shown in the right panel of Fig. 2, and derive a slope of 0.91 ± 0.09 with a RMS scatter of Σ_{SFR} about the fit of 0.35 dex, at 1.2 kpc scales. These results indicate that there are no significant differences in the KS parameters as a consequence of working at different resolutions, these agree well within the uncertainties of the data. As a result of averaging data at lower resolution, we see an expected decrease in the number of points that enter the fitting procedure, which increases the uncertainty of the fit. Consequently, this also effectively narrows the distribution, in good agreement with findings in previous studies of isolated galaxies (e.g., Bigiel et al. 2008; Schruba et al. 2010; Pessa et al. 2021).

The star formation efficiency of the molecular gas can be defined as the ratio between the traced rate of star formation and the amount of molecular gas that is available for star formation. In terms of our measured surface densities:

$$\mathrm{SFE}_{\mathrm{mol}} = \frac{\Sigma_{\mathrm{SFR}}}{\Sigma_{\mathrm{mol}}}. \tag{4}$$

Inversely, the molecular gas depletion time gives a quantitative estimate of the time necessary for a given region to consume the available gas if star formation remains constant at the present rate. It can be defined as

$$\tau_{\mathrm{dep}}^{\mathrm{CO}} = \Sigma_{\mathrm{mol}}/\Sigma_{\mathrm{SFR}}, \tag{5}$$

in the particular case in which the molecular gas is traced by CO. Conversely,

$$\tau_{\mathrm{dep}}^{\mathrm{CO}} = 1/\mathrm{SFE}_{\mathrm{mol}}. \tag{6}$$

In comparison with the mean depletion times of $\sim 2\,\mathrm{Gyr}$ found in Bigiel et al. (2008) and Leroy et al. (2013) for HERACLES, we derive a median H_2 depletion time of 1.8 Gyr for our full sample of VERTICO galaxies. These values are within the range of median depletion times in the PHANGS galaxies (1.18 to 2.10 Gyr, Utomo et al. 2018; Querejeta et al. 2021), but overall larger than the 0.6 Gyr derived from integrated values for the *Herschel* Reference Survey sample (Boselli et al. 2014). Our results are in reasonable agreement within uncertainties with the range of KS slopes found in previous studies (e.g., Bigiel et al. 2008; Usero et al. 2015; Lin et al. 2019; Ellison et al. 2021a; Pessa et al. 2021; Querejeta et al. 2021, see Table 2). The derived slopes at both resolutions are fully compatible within uncertainties to the slope of 1.0 found for the HERACLES samples used in Bigiel et al. (2008) and Leroy et al. (2013). It is important to note that the slope of the KS relation has been reported to vary significantly depending on the choice of CO-to-H_2 conversion factor, resolution, and the details of the fitting methodology employed (e.g., Leroy et al. 2013; Ellison et al. 2021a; Querejeta et al. 2021), as reflected in Table 2.

5.2. The KS relation in HI-deficient environments

It is well known that atomic gas in galaxies, which ultimately constitutes the fuel for molecular cloud formation, can be strongly affected by environmental processes. In particular, galaxies residing in clusters can often be HI-deficient, showing asymmetric or even truncated HI disks (Koopmann & Kenney 2004; Chung et al. 2009; Taylor et al. 2013; Yoon et al. 2017). HI-deficiency is thus a useful parameter that allows us to quantify the effects of environmental influence on cluster galaxies. These differences could directly affect the way star formation proceeds in those galaxy disks. In fact, over the past decade recent studies have shown that molecular gas can also be influenced by dynamical processes in the cluster (Vollmer et al. 2008; Fumagalli et al. 2009; Boselli & Gavazzi 2014; Zabel et al. 2019; Moretti et al. 2020). Furthermore, the recent VERTICO study described in Zabel et al. (2022) shows that the environmental mechanisms observed in the atomic gas can also affect the molecular gas reservoirs of cluster galaxies. In particular, galaxies with large HI deficiencies have steeper and more centrally concentrated molecular gas radial profiles.

In this study we differentiate between HI-normal galaxies (i.e., not affected by the environment) and HI-deficient galaxies. We do so by establishing a cut based on global HI-deficiencies calculated for VERTICO in Zabel et al. (2022; see their Table 1, column 10), using the predicted HI mass from field galaxies at fixed stellar mass. In this way, we consider HI-deficient galaxies as those with $\mathrm{def}_{\mathrm{HI},\,M_*} > 0.3$.

The left panel of Fig. 3 shows the ensemble resolved KS relation for HI-deficient galaxies (red contours) and normal galaxies (blue contours), allowing us to compare between the two families of galaxies in the sample. By using the same fitting methodology described in Sect. 5.1, we obtain a resolved KS slope of $N = 0.93 \pm 0.04$, a $\langle \log_{10} \Sigma_{\mathrm{SFR}}/\Sigma_{\mathrm{mol}} \rangle = -9.34 \pm 0.04$ and a 1-σ scatter of 0.30 dex for those galaxies classified as HI-deficient. In comparison, the resulting quantities for the HI-normal galaxies show a characteristic slope of $N = 0.84 \pm 0.04$,
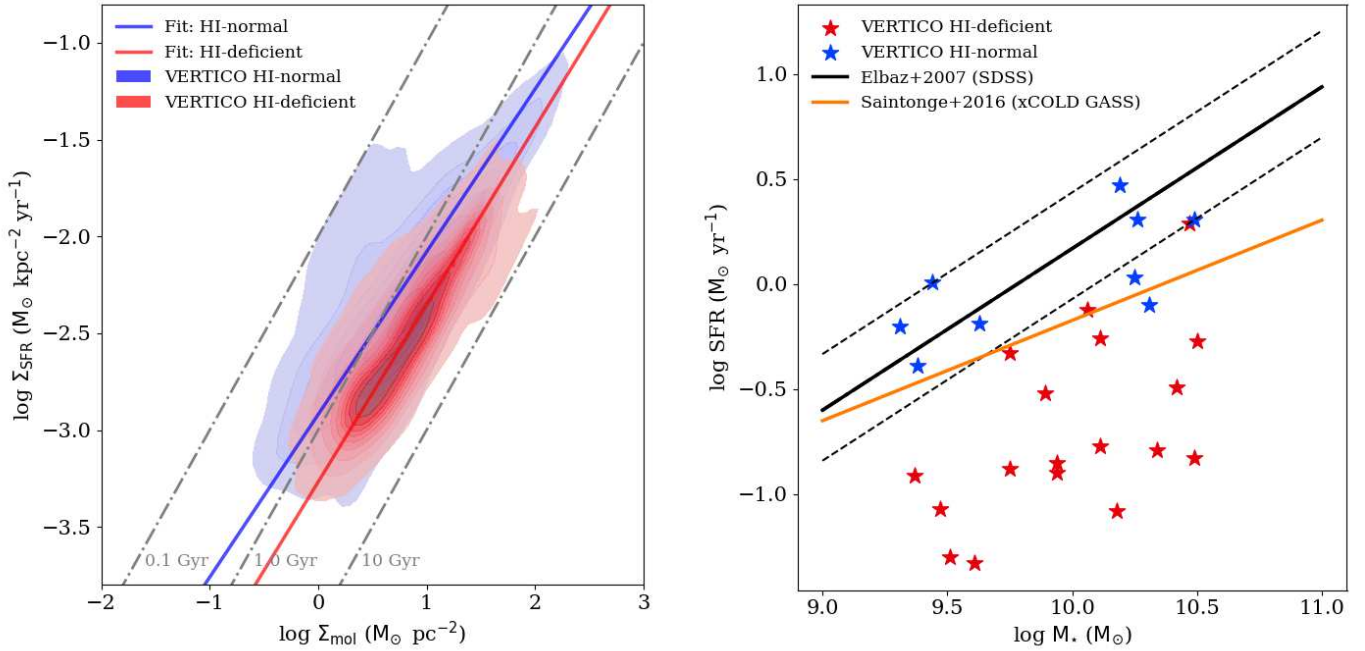
Fig. 3. *Left*: resolved KS relation for the VERTICO ensemble sample at a resolution of 720 pc. The red contours show the relation obtained for HI-deficient galaxies, according to Zabel et al. (2022), whereas the blue contours indicate the relation obtained for normal galaxies. Solid lines indicate LTS fits to the data. Similarly to Fig. 2 only galaxies with $i < 80°$ have been considered and values for Σ_{SFR} and Σ_{mol} have been corrected to face-on via cos$i$. The plot shows longer gas depletion times for HI-deficient VERTICO galaxies. *Right*: SFR $- M_{\star}$ relation for the VERTICO subsample, limited to HI-deficient and HI-normal galaxies covering the same range in stellar mass. The different colors indicate HI-deficient (red) and HI-normal (blue) galaxies. Overlaid are the star formation main sequence (SFMS) relation obtained in Elbaz et al. (2007) in black (solid line), as well as that presented in xCOLD GASS in orange (Saintonge et al. 2016). While VERTICO HI-normal galaxies lie on the SFMS, HI-deficient galaxies are mostly scattered below the SFMS.

a $\langle \log_{10} \Sigma_{SFR} / \Sigma_{mol} \rangle = -9.10 \pm 0.06$ and a 1-σ scatter of 0.41 dex. These two statistically different KS relations indicate that HI-deficient galaxies are offset toward more quiescent SFR surface densities by 0.23 dex. These differences clearly show that the resolved KS slope and star formation efficiency are moderately affected by the galaxy environment, in the sense that more HI-deficient galaxies tend to have steeper slopes and show lower molecular gas efficiency than HI-rich galaxies.

We compare these two samples of galaxies in the right panel of Fig. 3. This plot represents the SFR $- M_{\star}$ relation in VERTICO, limiting our sample to those HI-deficient and HI-normal galaxies covering the same range in stellar mass. This approach allows us to compare their properties more homogeneously. The blue data points indicate HI-normal (nondeficient) galaxies, whereas the red data markers represent the HI-deficient subsample of galaxies. The solid lines indicate the star formation main sequence (SFMS) relation obtained in Elbaz et al. (2007) in black, as well as that presented in xCOLD GASS in orange (Saintonge et al. 2016). The plot shows that VERTICO HI-normal galaxies lie on the SFMS, while HI-deficient galaxies are mostly scattered below the SFMS. HI-deficient galaxies also have global SFRs that are, on average, 0.60 dex lower than those of galaxies on the SFMS, for a fixed stellar mass.

We explore the potential correlation between the total stellar mass, the global SFR and the specific SFR (sSFR) as a function of HI-deficiency in Fig. 4. We measure the strength of the correlation between each pair of variables with the Pearson correlation coefficient. As a reference, coefficients ranging between 0.7 and 1.0 (-0.7 and -1.0) indicate a strong positive (negative) linear correlation. Values between 0.3 and 0.7 (-0.3 and -0.7) show a moderate positive (negative) correlation. Finally, Pearson coefficients between 0 and 0.3 (0 and -0.3) indicate

a weak positive (negative) linear relationship. The left panel shows that there is a weak correlation between HI-deficiency and stellar mass. However, we find that there is a moderate anticorrelation between HI-deficiency and the global and specific SFRs. These results indicate that the secular evolution, related to the galaxies' mass, is not the only factor driving the galaxies toward systematically lower values of SFR. On the contrary, the Virgo galaxies presented here are clearly being perturbed by environment-driven processes (e.g., Chung et al. 2009; Yoon et al. 2017; Brown et al. 2021; Boselli et al. 2022; Zabel et al. 2022). Our results show that these processes constitute an important factor in quenching galaxies by systematically lowering the star formation efficiency of the molecular gas. Our findings are directly related to the conclusions reported in Villanueva et al. (2022). This study finds a clear trend of lower molecular SFE for increasingly disturbed HI galaxy disks in Virgo. These findings are also in line with those found by Zabel et al. (2022). Quantities driving the HI morphology are also affecting the SFE in the molecular gas, without necessarily affecting the amount of molecular gas inside[ ] galaxy disks.

5.3. The KS relation for individual galaxies

Recent works (e.g., Lin et al. 2019; Ellison et al. 2021a; Pessa et al. 2021; Querejeta et al. 2021) have shown that there is a large galaxy-to-galaxy diversity in the observed KS scaling relations. In this section we explore the variety of KS relations among different galaxies, in particular in Fig. 5. These plots are analogous to Fig. 2, but each panel shows the resolved KS relation for each of the 37 galaxies in our VERTICO sub-sample. In all panels, each marker represents an individual measurement at
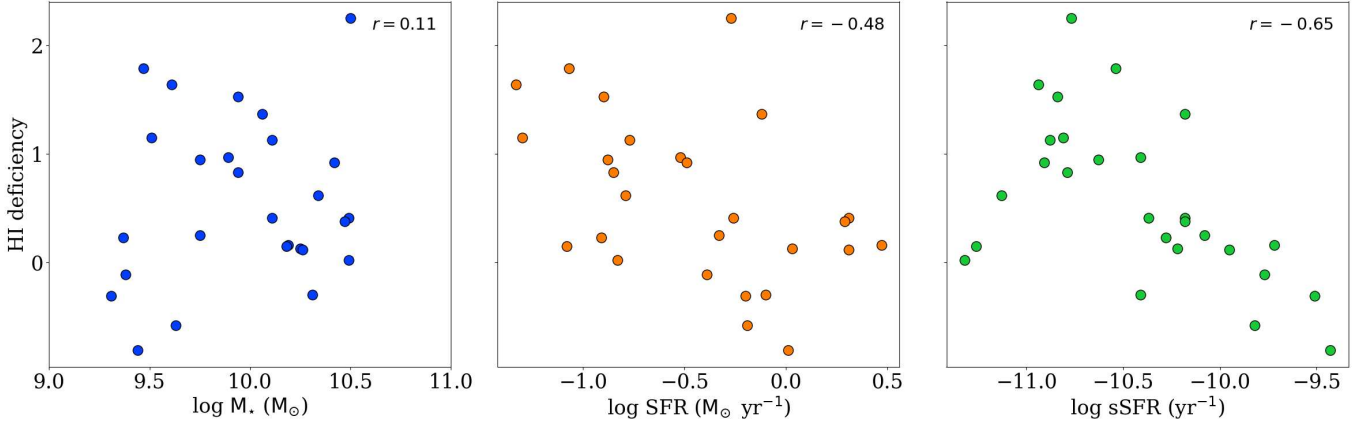
Fig. 4. HI-deficiency parameter as a function of the total stellar mass (*left*), global star formation rate (*middle*) and specific SFR (*right*) for each galaxy. The Pearson's correlation coefficients are shown on the different panels for each distribution. These quantities are calculated for the VERTICO sample of galaxies shown on the right panel of Fig. 3.
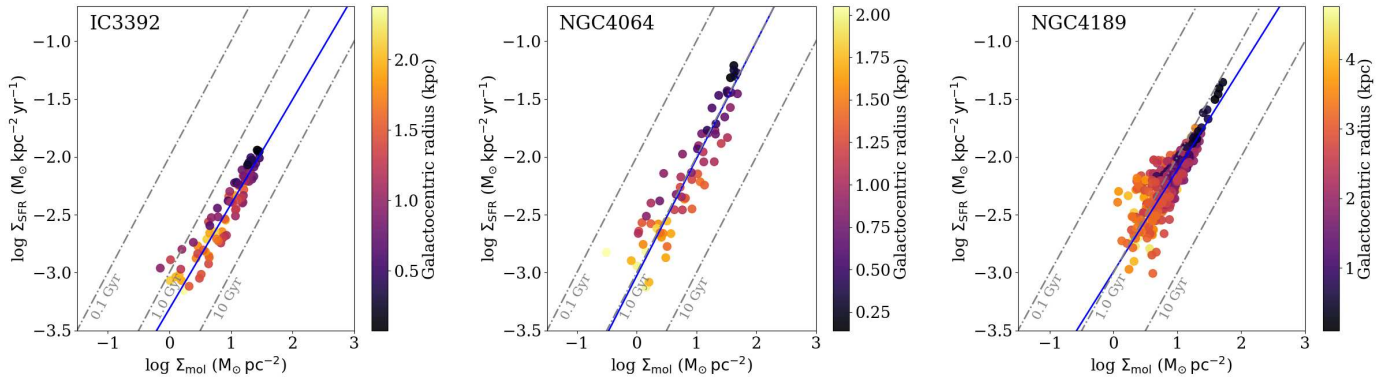
Fig. 5. The resolved Kennicutt-Schmidt relation for the sub-sample of galaxies in the VERTICO sample with inclinations $i \leq 80°$, represented as Σ_{SFR} as a function of Σ_{mol}. All data points are convolved to a common working resolution of 720 pc. Each data point is color-coded by the distance to the galaxy center. The diagonal dashed, grey lines show constant depletion times of 0.1, 1 and 10 Gyr, respectively. For a fixed molecular gas mass, there are clear galaxy-to-galaxy variations in the KS relation. OLS weighted fits to the line-of-sight measurements are the solid blue lines shown in Table A.1. Note that values for Σ_{SFR} and Σ_{mol} have been corrected via cos i. The rest of the panels can be found in Fig. A.1.

a common resolution of 720 pc, and they are color-coded by the galactocentric radius.

Similarly to what we describe in Sect. 5.1, we perform a robust LTS fit to each individual galaxy, shown as a solid blue line in each panel of Fig. 5. Table A.1 shows that the slopes obtained by fitting individual Σ_{SFR}-to-Σ_{mol} relations range between $N = 0.69$ and $N = 1.40$, with a mean typical scatter of ±0.21 dex. We note again that these uncertainties on the fitted variables do not reflect important systematic effects such as the choice of SFR tracer or a variable α_{CO} conversion factor.

When visually inspecting the panels, it is clear that there is significant galaxy-to-galaxy variation (take galaxies NGC 4457 and NGC 4713 as examples), confirming that there is no single resolved KS relation that can accurately describe every galaxy. Figure 5 visually demonstrates the second main conclusion of our work, that disk galaxies in VERTICO exhibit significant galaxy-to-galaxy variation in their KS relations. This result agrees with previous findings by studies using resolved molecular gas maps in isolated and cluster galaxies, such as Bigiel et al. (2008), Shetty et al. (2013, 2014), Ellison et al. (2020, 2021a), and Zabel et al. (2020). However, while we see that the slope and normalization vary from galaxy to galaxy, almost all of them show a strong, direct proportionality between Σ_{SFR} and Σ_{mol}. Both quantities appear to be related for most galaxies through

an index which is close to the $N = 1$ molecular KS law. In other words, the galaxies selected from the VERTICO survey contain molecular gas that appears to be forming stars at a nearly constant rate (or constant depletion times), although that rate can vary from galaxy to galaxy by a factor of ~4. This is one of the main sources of variations in the overall scatter we see in the resolved KS relation for the ensemble of galaxies, since galaxy-to-galaxy variations can account for a factor of ~0.20 dex scatter in the ensemble (with a total of 0.42 dex) sample (Ellison et al. 2021a).

Figure 6 shows the distribution of best-fit KS index for individual galaxies in VERTICO, as well as a comparison to other isolated galaxies in HERACLES (Leroy et al. 2013) and PHANGS (Pessa et al. 2021). We stress the message described above: while there is a clear variety of KS indexes from galaxy to galaxy, 76% of our targets' slopes are within the range of 0.8–1.2. This agrees with previous results showing that, to first order, the reservoir of molecular gas is the key quantity regulating star formation. While the slope index N is very close or compatible with unity, we note that the majority of our sample (about 67%) is characterized by sublinear slopes. This could be the result of a possible dependence on the assumed constant α_{CO}. Given that both metallicity and gas column density can decrease radially across galaxy disks, the slope of this KS relation can be
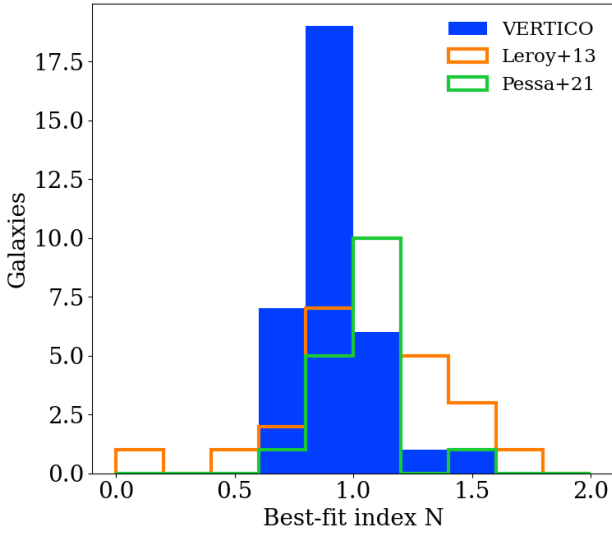
Fig. 6. Histogram of best-fit power-law KS index, N, for individual galaxies in VERTICO (blue color, see Table A.1) using a fixed CO-to-H_2 conversion factor. For a comparison, orange bars represent the sub-sample of HERACLES galaxies used in Leroy et al. (2013) and green bars show the best-fit slopes found for the sub-sample of PHANGS galaxies presented in Pessa et al. (2021). The distribution of best-fit N for individual galaxies in VERTICO spans the range $N \sim 0.7-1.5$ and peaks near $N = 0.9$, while this value is slightly larger for the HERACLES and PHANGS distributions.

modified as a result. On the other hand, this could also indicate that the star formation efficiency of the molecular gas tends to decrease at high molecular gas densities for most of the galaxies. A variable molecular gas star formation efficiency is also evident in the significant scatter we see for each individual KS relation, indicating that the Σ_{SFR}-to-Σ_{mol} relation varies not only from galaxy to galaxy, but also within galaxies. This reflects the broad variety of physical conditions presented in Virgo galaxies. Some cases are particularly interesting, such as NGC 4561 and NGC 4772. Figure 5 shows that the KS relation seems to break for these galaxies at face value, and therefore a power-law description is not a good approximation. It is important to note that these two targets are not representative of the full sample, since they have been marginally detected in CO in VERTICO (see Brown et al. 2021). Their integrated intensity maps show a very small dynamic range in Σ_{mol} up to $\sim 5-7\, M_\odot\, pc^{-2}$. This is also evident by the limited radial profiles shown in Brown et al. (2021), where only a few detections are available in the inner regions of the galaxies disks ($r < 6\, kpc$).

There are two additional galaxies, NGC 4501 and NGC 4579, which present a clear bimodal behavior for different galactic environments. Figure 5 indicates that their galaxy centers, within approximately 1.5 kpc, are characterized by much larger depletion times than those seen in their overall disks ($r > 1.5\, kpc$). Their centers, therefore, appear to follow a parallel KS relation to their disks. We note that these galaxies' central dynamics are particularly striking, as displayed in the velocity fields and position-velocity (PV) diagrams available in Brown et al. (2021).

There are several possible explanations behind the central deviation of τ_{dep} in NGC 4501. First, its central kinematics show signatures of outflowing material (Wong et al. 2004; Repetto et al. 2017), likely due to elliptical streaming, and this galaxy hosts a central AGN (Brum et al. 2017; Ruschel-Dutra et al. 2021). The presence of central AGNs has

been shown to affect the molecular gas reservoirs in the central regions of galaxies (Ellison et al. 2021b; García-Burillo et al. 2021). If the central molecular gas is outflowing, the standard Galactic conversion factor may not be applicable in this case, since the gas is not likely to be self-gravitating. Previous attempts to constrain molecular outflow conversion factors suggest that they could be two to four times below our constant Galactic value (Weiß et al. 2005; Cicone et al. 2012, 2018; Leroy et al. 2015; Zschaechner et al. 2018; Lutz et al. 2020). Such a decrease in the conversion factor would also drive the central molecular gas surface densities to values two to four times lower, which could explain the difference in τ_{dep} observed. In addition to that, this system has a clear bar which can drive noncircular motions in the molecular gas, acting to stabilize against star formation. Both the outflow and the bar can contain gas that may not be participating in the formation of new stars, as indeed is expected given that the large injected energies prevent it from collapsing and forming molecular clouds. Second, the center of NGC 4501 is characterized by abundant older stellar populations which suggest a weaker star-forming activity. An inferred lower Σ_{SFR} in its central region would cause a visible vertical drop in the KS relation toward longer depletion times. Both of these effects will cause an observed shift toward lower Σ_{SFR} and larger Σ_{mol}. Finally, HI emission maps and simulations (Vollmer et al. 2008; Chung et al. 2009) have recently shown that NGC 4501 is also undergoing early phases of ram pressure stripping. This could potentially drive the central galaxy away from the KS relation in its disk. Similarly to NGC 4501, NGC 4579 has a low-luminosity AGN in its center (Kuno et al. 2007) and a compact inner nuclear ring that could help increase the molecular gas densities in its central region. However, it is challenging to estimate how the presence of a central AGN would affect the calculated SFRs, since it could directly affect both WISE3 and WISE4 filters differently, and therefore the color correction. In the presence of an AGN, the SFR derived using a combination of UV and IR tracers is likely inaccurate.

It is also interesting to point out the pair of interacting galaxies NGC 4567 and NGC 4568. While both galaxies seem to be well characterized by a sublinear KS slope, this pair of spiral galaxies overlap in the sky. In this case it is difficult to differentiate the components of each disk, since their line-of-sight velocities match in the overlapping region. Their HI emission maps (Chung et al. 2009) show that they are physically connected and interacting gravitationally, which could potentially explain the suppression of the SFR seen in the low molecular gas surface density regions of NGC 4568. Nehlig et al. (2016) studied in detail the influence of large-scale compression ($\sim$kpc scales) on density, molecular fraction and molecular SFE based on IRAM-30m CO (2-1) observations. In agreement with our higher resolution data, they also report a $0.9-1.0$ KS index. They also find lower SFE of the gas in the northwestern interacting part of the galaxies, as well as in the southwestern edge of NGC 4568. They conclude that gravitational ISM compression can justify an increase in gas surface densities as well as molecular fractions, which could potentially explain the observed changes in SFE. In that context, a recent study by Thorp et al. (2022) analyses the resolved molecular gas and star formation properties in a large set of galaxy mergers at different stages of interaction. While they find that scaling relations in post-mergers, pairs and isolated galaxies are similar, there is significant variation in individual mergers.

As described above, the entire VERTICO survey comprises a total of 51 Virgo Cluster galaxies, with a significant

fraction of highly inclined disks. While these galaxies have not been taken into account in our analysis, we provide an overview of all KS relations in Fig. B.1, using direct observables (e.g., I_{CO}).

5.4. Star Formation Efficiencies in VERTICO

Our results can additionally be analyzed in terms of the star formation efficiency of the molecular gas, SFE_{mol} or, conversely, in terms of the depletion time τ_{dep} as defined in Sect. 5.1. VERTICO allows us to resolve different regions within galaxy disks, so that we can explore dependencies of the depletion times as a function of the local environment.

While combining our measurements into a single dataset is helpful to understand the ensemble tendencies of our galaxies, it can obscure real trends and differences among them. Figure 5, together with our measurements in Table A.1 show systematic variations in the power-law index among galaxies, as well as in their median τ_{dep} values from galaxy-to-galaxy. In addition, we also encounter large internal variations in the depletion times for the majority of the sources, as reflected by the individual mean scatter of ±0.21 dex. This is also evident by the large scatter we see at fixed molecular gas surface densities in Fig. 5, which spans almost an order of magnitude. Clear examples of a varying τ_{dep} are NGC 4383, NGC 4501, NGC 4579 and NGC 4654. Two of them, NGC 4501 and NGC 4579, have particularly active and AGN-dominated centers.

In addition to systematically quenching the star formation rates in highly perturbed systems, as seen in Fig. 3, the cluster environment in which VERTICO galaxies live can also influence the resolved physical properties of the atomic and molecular gas within its disk through gravitational and/or hydrodynamic interactions. This could therefore favor local regions of gas compression through external interactions which may, in turn, create gradients or enhanced regions of star formation. We explore whether such regions exist in the disks of our VERTICO subsample by studying azimuthal variations of the measured SFE in the molecular gas. We start by taking the center of each galaxy to be its optical center. We sample each galaxy with 18 radial vectors in the RA-DEC plane. For each vector we calculate the angular separation to each pixel in the computed SFE map (Fig. 7, middle). We select the angle which by eye most cleanly creates a divergent distribution in SFE by azimuthal angle, as shown in our resolved KS plot, color coded by the different angular offsets (Fig. 7, bottom).

Figure 7 shows example plots for two galaxies, NGC 4383 and NGC 4654, where these azimuthal variations are found to be the strongest in VERTICO. The top panels show integrated intensity maps of the ^{12}CO (2–1) emission in both galaxies. In each intensity map, the black dashed arrow shows the reference direction from which angular offsets are measured for each different line-of-sight in the galaxy disk. Angular offsets are always measured starting from the arrow to each different point in the galaxy disk, and therefore range from 0° to 180°. The middle panels show a resolved map of the SFE of the molecular gas in each galaxy. The bottom panels in Fig. 7 present the individually resolved KS relation, Σ_{SFR} as a function of Σ_{mol}, where each data point is color coded by the angular separation computed from the reference direction marked in the left panel.

As seen in the bottom panels of Fig. 7, the colors help us visualize that regions located at different angular distances from a preferred direction follow slightly different KS relations. For NGC 4654, the split in colors is more evident for the direction as drawn in the bottom right panel of Fig. 7. This direction coin-

cides with the direction of interaction with the companion galaxy NGC 4639 (see Vollmer 2003; Lizée et al. 2021, Fig. 1), which caused the molecular gas to be asymmetrically distributed along the major axis of the galaxy. Figure 7 shows that disk regions within ~70° from the direction of interaction tend to follow a KS relation characterized by slightly longer depletion times (~0.9 Gyr) than those regions in the opposite side (~0.5 Gyr). These results appear to be in agreement with previous results reported by Lizée et al. (2021). Using new CO (2–1) data from the IRAM-30m telescope, the authors find an enhanced SFE, and therefore shorter depletion times, in the NW region of the galaxy, coincident with an arm of high molecular gas surface density and stellar surface densities. Through their observations and consequent modeling of the data, they hypothesize that this molecular gas surface density must have been enhanced after a period of time where the gas was being compressed through the interaction with NGC 4639. This gas compression then led to increasing the SFR and the turbulent velocity of the region, giving rise to elevated efficiencies of the molecular gas.

In the case of NGC 4383 we see both radial and azimuthal variations in the depletion time. The left panels of Fig. 7 show that regions with angular separations within ~80−120° (therefore perpendicular to the preferred direction) tend to follow a super linear KS relation characterized by longer depletion times. The region along the semi-minor axis of the galaxy shows much higher star formation efficiencies, with median depletion times of ~0.4 Gyr. As previous studies pointed out (see e.g., Koopmann & Kenney 2004; Chung et al. 2009), NGC 4383 is an amorphous starburst galaxy characterized by powerful outflow and bright Hα and UV emission in its central region, with global SFR that are typically 2–3 times higher than any other isolated field galaxies of similar luminosity. The origin of this starburst-related outflow is still unclear. However, these elevated central SFRs have been argued to be a consequence of cluster interactions, likely to be the result of tidal interactions and gas accretion (Chung et al. 2009).

6. Discussion

6.1. Kennicutt-Schmidt in Virgo

The relation between molecular gas surface densities and SFR surface densities is one of the best studied galaxy scaling relations. It helps us quantify the relative changes in star formation rate, as a consequence of variations in the resolved molecular gas mass. In particular, it is critical to constrain the slope of this relation since it is often used in the typical star formation prescriptions adopted in semi-analytic models or in resolved 2D models of galaxy evolution. A one-to-one correlation between these quantities is indicative of the molecular gas being the necessary fuel for star formation to occur, where gas is converted into stars at a constant efficiency of molecular gas. Steeper slopes indicate enhanced star formation for high molecular gas surface densities. A sublinear slope, on the contrary, indicates that the observed depletion times for molecular gas increase at higher molecular gas surface densities.

The results we present in this work are in-line with previous studies (see Table 2 for a brief summary) where a KS relation with a slope of $N \sim 1$ has been determined (e.g., Bigiel et al. 2008; Schruba et al. 2011; Leroy et al. 2013; Usero et al. 2015; Ellison et al. 2021a). For the ensemble VERTICO sample of galaxies we derive a slightly sublinear slope of 0.97 ± 0.07, compatible with a linear KS relation within uncertainties. This implies that, globally, the VERTICO galaxies convert molecular
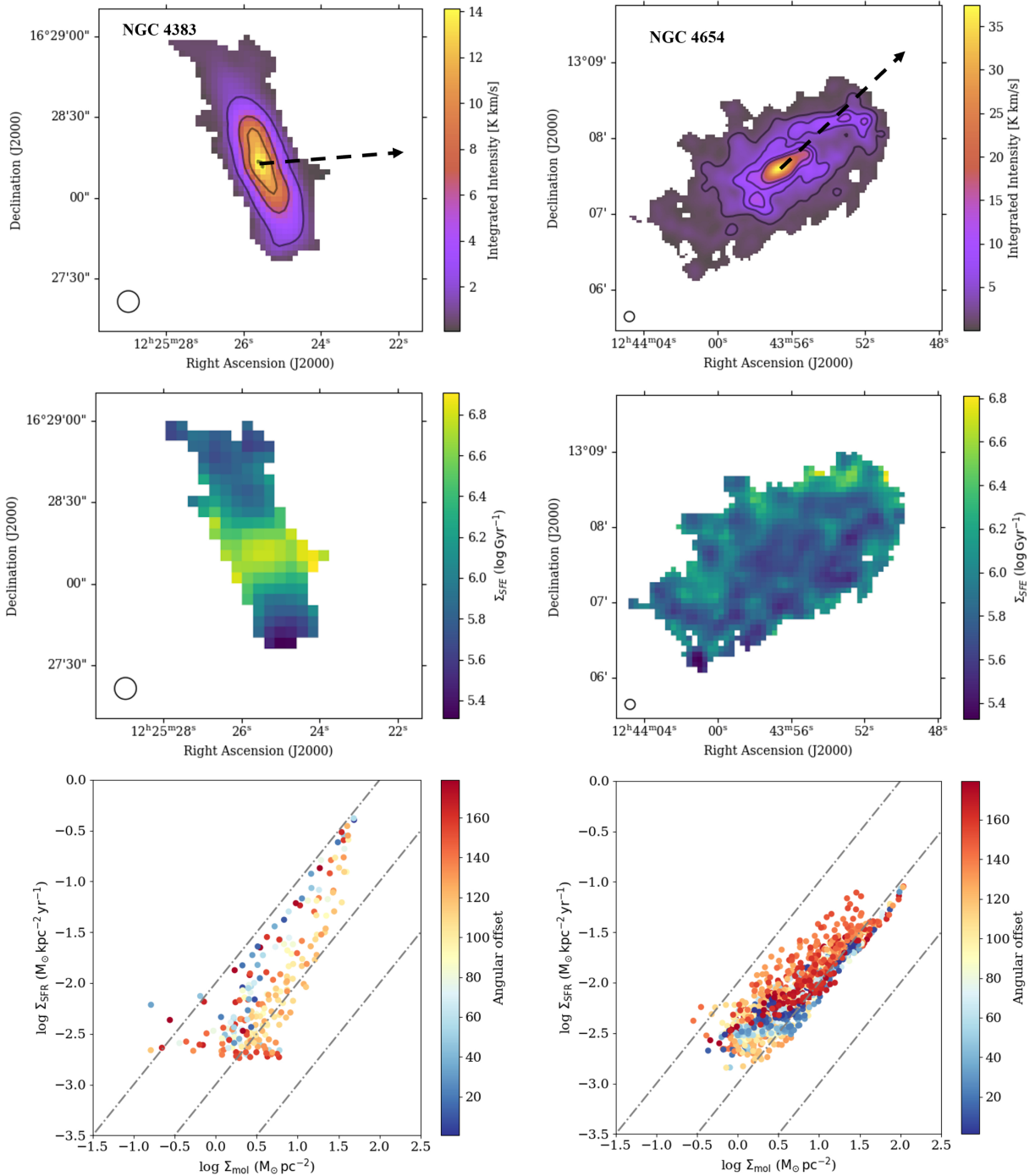
Fig. 7. Systematic azimuthal variation of SFE. *Top*: integrated intensity map of CO (2–1) emission for NGC 4383 (*left panel*) and NGC 4654 (*right panel*). The black dashed arrow represents the direction where the largest azimuthal variations of SFE are found. Angular offsets are measured from this direction to each different line-of-sight. *Middle*: Map of resolved star formation efficiency of molecular gas, calculated as shown in Eq. (4). *Bottom*: Resolved Kennicutt-Schmidt relations, color coded by the angular separation from the preferential direction shown on the integrated intensity map.

gas into stars at a roughly constant efficiency across their disks, and agrees with previous findings in that the KS relation is more linear than its atomic version (Bigiel et al. 2008; Leroy et al. 2013). We also find a median $\tau_{\rm dep}$ = 1.86 Gyr for our full sample, which is well within the range of typical values found in nearby, star-forming galaxies (∼1−3 Gyr, see Bigiel et al. 2008; Leroy et al. 2008, 2013; Rahman et al. 2012; Querejeta et al. 2021). It is important to note that we observe significant scatter, both within and among galaxies.

While the VERTICO galaxies selected for this study live in a cluster of galaxies, their KS slopes and median depletion times largely overlap with those observed by Bigiel et al. (2008) and Leroy et al. (2013) in isolated galaxies, as seen by the HERACLES survey data. While such a direct comparison might suggest that the denser cluster environment does not alter the molecular gas reservoirs in a way that alters the global star formation properties of galaxy disks, molecular gas can be affected by hydrodynamic pressure exerted by the hot

intracluster medium (Tonnesen & Bryan 2009; Lee et al. 2020). A clear example is the direct observational evidence of molecular gas found to be stripping via ram pressure in galaxy clusters. Some of the first observations to confirm that are in the Norma cluster (Jáchym et al. 2014), in Virgo (Verdugo et al. 2015) and the Coma cluster (Jáchym et al. 2017). The work by Zabel et al. (2019) has recently presented clearer evidence of molecular gas stripping in the Fornax cluster, where CO is detected in extended tails from several late-type galaxies. It is important to note that the Virgo cluster, however, is much sparser, spiral-rich, and X-ray faint than some clusters. In comparison, the Coma cluster only contains ~15% of spiral galaxies.

Our VERTICO results also agree with previous observations by Zabel et al. (2020) in Fornax cluster galaxies, where the authors find that the overall KS relation is similar to those found by Kennicutt (1998) and Bigiel et al. (2008), but show slightly shorter depletion times due to the presence of dwarf galaxies with disturbed molecular gas. Numerical simulations (e.g., Di Matteo et al. 2007) already pointed out that galaxy interactions do not necessarily translate into a more efficient conversion of molecular gas into new stars. Overall, they find that all stages of interaction can follow the same general KS sequence. On the other hand Roediger & Brüggen (2007, 2008) also simulated ram pressure in cluster galaxies, which could lead to enhanced episodes of star formation on the leading side of some galaxies experiencing mild ram pressure, as observed in NGC 4654.

The KS slopes for the vast majority of our sample, are lower than unity. Sublinear slopes indicate that the molecular gas depletion time increases with increasing gas surface density. Such sublinear slopes have been actively debated in previous works (e.g., Shetty et al. 2013, 2014) and could simply indicate that, on average, not all the CO-traced molecular gas is associated with star formation. The CO measurements could instead include a more diffuse phase (Rahman et al. 2011; Pety et al. 2013), while star formation is only taking place in the densest regions (e.g., Gao & Solomon 2004), such that CO emission does not correlate with star formation activity on a one-to-one relation.

The VERTICO galaxies analyzed here also exhibit significant scatter in their resolved relations between Σ_{SFR} and Σ_{mol}. This suggests that there is no single characteristic τ_{dep} for all the galaxies, but rather a systematic variation of individual depletion times on subgalactic scales. This result is also in agreement with findings in local galaxies (Bigiel et al. 2008; Leroy et al. 2013; Shetty et al. 2014; Utomo et al. 2017; Ellison et al. 2021a) and cluster members (Zabel et al. 2020). Therefore Σ_{SFR} must depend on other internal environmental properties besides molecular gas surface densities such as turbulence, metallicity, or gas fractions, among others. In some of our galaxies, we are able to attribute individual variations in the depletion times to a likely distinct behavior in the galaxy centers of NGC 4501 and NGC 4579, as well as tidal interactions and ram-pressure stripping in galaxies NGC 4383 and NGC 4654, respectively.

6.2. Fitting methodology and sample

Several caveats and assumptions may have an impact in our derived slopes, and we warn the readers that comparisons among different observations and studies should be done with caution. One of the factors introducing large discrepancies in the KS slopes revolves around the fitting techniques employed. Various fitting methodologies can effectively yield very different KS parameters (Leroy et al. 2013; de los Reyes & Kennicutt 2019). In particular, Ellison et al. (2021a) find significant differences between the ODR and OLS fitting procedures in the ALMaQUEST (ALMA MaNGA Quenching & Star-Formation) survey, resulting in super-linear and sub-linear KS relations respectively, as well as in different mean depletion times. These differences are also evident from Table 2, where the fitting approach varies significantly. It is worth noting that interpreting the results from simple bisector and OLS regressions is statistically hard, since a linear slope could even result from a scenario where there is no correlation between a predictor and its response (see e.g., Isobe et al. 1990; Shetty et al. 2014).

The slope of the KS relation can also be affected by the choice of α_{CO}. While we have adopted a constant value in this work, it is well known that the CO-to-H_2 conversion factor varies within and among galaxies. Not only it has been found to decrease in regions with very high values of SFR (Downes & Solomon 1998; Bryant & Scoville 1999), but also galaxies tend to have lower CO-to-H_2 conversion factors in their central regions (Sandstrom et al. 2013) when compared to their outskirts. In addition, it is inversely correlated with metallicity (e.g., Wilson 1995; Genzel et al. 2012; Bolatto et al. 2013; Accurso et al. 2017; Sun et al. 2020). As an example, Querejeta et al. (2021) show that there is a significant variation (about ~30%) in the slopes and intercepts derived for the KS relation in the PHANGS sample, depending on the adopted α_{CO} conversion factor, with galaxy centers being the most sensitive environment. In particular, they quote KS slopes ranging between 0.90 ± 0.05 and 1.43 ± 0.27 for the overall disks. Additionally, Pessa et al. (2021) explores the impact of assuming a constant conversion factor, rather than a metallicity dependent one, on their measured KS relationship in PHANGS, finding a decrease of ~5% in the KS slope. In addition, they point out that the timescales probed by the SFR prescription strongly impacts the resulting KS parameters. In particular, they find that a longer timescale SFR tracer pushes previously low SFRs to higher values, which results into a significant flattening of the KS slope (from 1.06 ± 0.01 to 0.60 ± 0.01).

An additional concern to the fitting methodology employed is that it uses the same weighting scheme for every sampled region in our galaxies. Therefore it could be expected that galaxies with more extended H_2 disks (i.e., those less affected by the environment) and a larger number of resolved regions could be dominating the ensemble fit, driving the slope of the KS relation. As an example, NGC 4254 and NGC 4321 are two of the more extended VERTICO galaxies, typically considered as normal galaxies (see e.g., Pessa et al. 2021), and would be expected to dominate the KS slope and scatter. We address this issue by weighting each line-of-sight measurement by the number of independent measurements that a given galaxy contributes to the overall sample, as also described in Zabel et al. (2020). Following this procedure, we obtain a resolved KS slope of $N = 0.99 \pm 0.02$, with a median $\log_{10}\Sigma_{SFR}/\Sigma_{mol} = -9.25 \pm 0.06$ and a 1-σ scatter of 0.40 dex. While this result provides a slope that is more representative of every galaxy, it also shows that the slope is effectively the same as that derived in Fig. 2 within the measured uncertainty range.

6.3. Environmental influence on the resolved KS relation

It is clear that environment is a key element shaping galaxy evolution. Clusters of galaxies are particularly interesting environments to study extreme and unusual ISM properties in galaxy disks. These rich environments can perturb both the atomic and molecular gas content, especially through ram pressure stripping of the gas, and thus drastically affecting their evolution. A large

number of observational studies have shown that cluster galaxies tend to have lower atomic (e.g., Haynes & Giovanelli 1984; Cayatte et al. 1990; Catinella et al. 2013) and molecular (e.g., Fumagalli et al. 2009; Boselli & Gavazzi 2014) gas content than field galaxies. In this context, VERTICO aims to systematically uncover the links between resolved molecular gas and star formation in a large sample of late-type cluster galaxies.

RPS is one of the most important perturbations in cluster environments, and generally considered as the dominant process in rich galaxy clusters (e.g., Vollmer et al. 2001; Boselli & Gavazzi 2006; Boselli et al. 2014). During this process, the ISM of galaxies, especially in the outer parts of their disks, is removed by the external pressure or due to its friction with the ICM. Both the atomic gas and the molecular gas (less severely) can be stripped during the interaction. As a consequence, the denser molecular gas component, within giant molecular clouds, also decreases since it cannot longer be replenished by the diffuse gas component (Tonnesen & Bryan 2009). In these cases, the star formation activity in those galaxies is also affected as they slowly consume the available gas reservoir (Boselli & Gavazzi 2014). In this context, the HI-deficiency parameter can be used as an indirect tracer of perturbed environments in statistical studies (e.g., Haynes & Giovanelli 1984; Solanes et al. 2001; Gavazzi et al. 2005, 2006; Catinella et al. 2013; Loni et al. 2021). The works by Fumagalli et al. (2009) and Boselli & Gavazzi (2014) have additionally shown that the molecular gas content tends to decrease in perturbed, HI-deficient galaxies. This indicates that hydrodynamical processes like RPS can directly affect the cold, dense molecular gas component (Wilson et al. 2009; Mok et al. 2016; Chung et al. 2007) and ultimately reduce the star formation activity, as previously observed in nearby clusters (e.g., Kennicutt 1983; Moss & Whittle 1993; Gavazzi et al. 2006; Haines et al. 2007; Vulcani et al. 2010).

The results presented in Sect. 5 show the same trend for Virgo cluster galaxies in a systematic way: HI-deficient galaxies tend to have a reduced global star formation activity and lower star formation efficiency of their molecular gas. This overall decrease of star formation situates the HI-deficient galaxies below the main sequence relation shown in the right panel of Fig. 3, compared to unperturbed galaxies which are scattered around it. The HI-deficiency parameter is a good proxy for environmental influence, therefore our results suggest that cluster environment is largely responsible for lowering the SFE in HI-deficient galaxies. These results are comparable to those found in Davis et al. (2014) for the ATLAS 3D Project galaxies, where early type galaxies (ETGs) are systematically found offset from the KS relation for normal and starburst galaxies. ETGs, which are typically far more HI-deficient than late-type galaxies (e.g., Huchtmeier & Richter 1989), show lower star formation efficiencies of the gas by a factor of ~2.5. While both results are not directly comparable, since Davis et al. (2014) employ total gas surface densities rather than just molecular gas surface densities, they point toward a key role of the gas dynamics to regulate star formation in galaxies.

In this context, our results are in agreement with recent efforts to characterize the atomic and molecular gas in Virgo cluster galaxies. A first piece of evidence is presented in Zabel et al. (2022), showing the effects of cluster environments in the VERTICO sample of galaxies. They find that VERTICO HI-deficient galaxies appear to have more compact molecular gas profiles, and indicate that these are a consequence of the same processes that act on the atomic gas removal via ram pressure stripping. In addition, they find a weak correlation between global HI and H_2 deficiencies, with galaxies that are HI-deficient because of their lower HI surface densities also being the most H_2 deficient (see Fig. 2 from Zabel et al. 2022 for a detailed summary). This weak correlation between HI and H_2 deficiencies indicates that environmental effects removing HI from galaxies also affect the molecular gas, albeit to a lesser extent. Similarly, Villanueva et al. (2022) note that VERTICO galaxies show a less extended molecular gas emission compared to their stellar distribution. In comparison to isolated galaxies, they find that these cluster galaxies have elevated molecular-to-atomic gas ratio and lower SFE of their molecular gas. Our results contribute to these major VERTICO efforts, providing additional evidence that the Virgo cluster environment affects the distribution and physical properties of the molecular gas, and its efficiency to form stars in such disturbed environments. We have shown the importance of environment in reducing the star formation efficiency of molecular gas. Future work will explore which mechanisms are most responsible and where, as well as how efficiency interacts with gas fueling to regulate the star formation cycle.

7. Summary and conclusions

In this work we employ new data for 37 spiral galaxies included in the ALMA large program VERTICO. These observations were used to investigate the resolved properties of the molecular gas and, combined with tracers of star formation activity, they allowed us to explore the resolved scaling relation between Σ_{SFR} and Σ_{mol}, known as the resolved KS relation, for the first time in a sample of star-forming galaxies within a cluster. In order to assess the universality of the KS relation, we explored the ensemble and individual scaling relations, and compared our results to a controlled sample of field, isolated galaxies from the HERACLES survey. Our main results are the following:

1. We confirm a strong correlation between Σ_{SFR} and Σ_{mol} at a linear resolution of 720 pc for the ensemble of galaxies, with a mean slope of $N = 0.97 \pm 0.07$, and a characteristic median depletion time of $\tau_{dep} = 1.86$ Gyr for our full sample. Our measurements agree well with those seen in previous work in isolated, star-forming galaxies in HERACLES (Bigiel et al. 2008; Leroy et al. 2013) and other surveys of resolved molecular gas emission (Schruba et al. 2011; Usero et al. 2015; Lin et al. 2019; Pessa et al. 2021; Querejeta et al. 2021). This suggests that, overall, star formation in the Virgo cluster operates in a similar way to that seen in isolated galaxies.

2. In individual galaxies, the derived KS parameters vary from galaxy to galaxy. We find slopes that range between 0.69 and 1.40, with a mean typical scatter of ±0.21 dex. and typical star formation efficiencies of molecular gas that can vary from galaxy to galaxy by a factor of ~4. This confirms that there is no single KS relation that can accurately describe every galaxy, as has been seen in previous studies (Bigiel et al. 2008; Saintonge et al. 2011; Shetty et al. 2013; Zabel et al. 2020; Ellison et al. 2021a).

3. While the ensemble KS relation strongly correlates Σ_{SFR} and Σ_{mol} for the full sample, there is almost an order of magnitude variation in the observed scatter for the entire sample. Compared to the scatter in the individual KS relations, galaxy-to-galaxy variations appear to account for approximately half of the scatter seen in the ensemble KS relation. In addition, the large scatter seen in depletion times inside individual galaxies (~0.23 dex) indicates that there are systematic variations at subgalactic scales, suggesting that Σ_{SFR}

may also depend on other local environmental properties besides molecular gas surface densities.

4. We observe clear azimuthal variations of the molecular gas depletion times in two of our galaxies, NGC 4383 and NGC 4654. These can be directly linked to the presence of gravitational tidal interactions and ram-pressure stripping of the gas, respectively, and provide additional evidence that the cluster environment directly affects the resolved physical properties of the molecular gas.

5. Using the HI-deficiency parameter as a proxy for cluster environment influence on the VERTICO sample, we find that the HI-deficient galaxies in the Virgo cluster show a steeper resolved KS relation and lower molecular gas efficiencies than HI-normal cluster galaxies. When comparing these subsamples of galaxies in the SFR-M_* plane, we find that HI-normal galaxies tend to lie over the SFMS, while HI-deficient galaxies have average global SFRs that are systematically lower by ∼0.60 dex, for a fixed stellar mass.

In conclusion, our observations highlight the important role of the cluster environment within and across cluster galaxies in Virgo. Our work evidences that the environmental mechanisms affecting the HI galaxy content also have a direct impact on the local molecular gas content and its star formation efficiency, which are reduced in HI-deficient cluster galaxies. This efficiency suppression in perturbed galaxies results in the systematic quenching of the SFR, eventually leading to longer depletion times in HI-deficient members.

References

Accurso, G., Saintonge, A., Catinella, B., et al. 2017, MNRAS, 470, 4750
Aniano, G., Draine, B. T., Gordon, K. D., & Sandstrom, K. 2011, PASP, 123, 1218
Bigiel, F., Leroy, A., Walter, F., et al. 2008, AJ, 136, 2846
Blanc, G. A., Heiderman, A., Gebhardt, K., et al. 2009, ApJ, 704, 842
Bloemen, J. B. G. M., Strong, A. W., Mayer-Hasselwander, H. A., et al. 1986, A&A, 154, 25
Bolatto, A. D., Wolfire, M., & Leroy, A. K. 2013, ARA&A, 51, 207
Bolatto, A. D., Wong, T., Utomo, D., et al. 2017, ApJ, 846, 159
Boquien, M., Lisenfeld, U., Duc, P. A., et al. 2011, A&A, 533, A19
Boselli, A., & Gavazzi, G. 2006, PASP, 118, 517
Boselli, A., & Gavazzi, G. 2014, A&ARv, 22, 74
Boselli, A., Lequeux, J., & Gavazzi, G. 2002, Ap&SS, 281, 127
Boselli, A., Lequeux, J., & Gavazzi, G. 2004, A&A, 428, 409
Boselli, A., Cortese, L., Boquien, M., et al. 2014, A&A, 564, A67
Boselli, A., Fossati, M., & Sun, M. 2022, A&ARv, 30, 3
Brown, T., Wilson, C. D., Zabel, N., et al. 2021, ApJS, 257, 21
Brum, C., Riffel, R. A., Storchi-Bergmann, T., et al. 2017, MNRAS, 469, 3405
Bryant, P. M., & Scoville, N. Z. 1999, AJ, 117, 2632
Buat, V. 1992, A&A, 264, 444
Cappellari, M., Scott, N., Alatalo, K., et al. 2013, MNRAS, 432, 1709
Catinella, B., Schiminovich, D., Cortese, L., et al. 2013, MNRAS, 436, 34
Cayatte, V., van Gorkom, J. H., Balkowski, C., & Kotanyi, C. 1990, AJ, 100, 604
Chung, E. J., & Kim, S. 2014, PASJ, 66, 11
Chung, A., van Gorkom, J. H., Kenney, J. D. P., & Vollmer, B. 2007, ApJ, 659, L115
Chung, A., van Gorkom, J. H., Kenney, J. D. P., Crowl, H., & Vollmer, B. 2009, AJ, 138, 1741
Cicone, C., Feruglio, C., Maiolino, R., et al. 2012, A&A, 543, A99
Cicone, C., Severgnini, P., Papadopoulos, P. P., et al. 2018, ApJ, 863, 143
Colombo, D., Hughes, A., Schinnerer, E., et al. 2014, ApJ, 784, 3
Cortese, L., Catinella, B., & Smith, R. 2021, PASA, 38, e035a
Cramer, W. J., Kenney, J. D. P., Cortes, J. R., et al. 2020, ApJ, 901, 95
Cramer, W. J., Kenney, J. D. P., Tonnesen, S., et al. 2021, ApJ, 921, 22
Daddi, E., Elbaz, D., Walter, F., et al. 2010, ApJ, 714, L118
Davis, T. A., Young, L. M., Crocker, A. F., et al. 2014, MNRAS, 444, 3427
de los Reyes, M. A. C., & Kennicutt, R. C. Jr. 2019, ApJ, 872, 16
den Brok, J. S., Chatzigiannakis, D., Bigiel, F., et al. 2021, MNRAS, 504, 3221
Di Matteo, P., Combes, F., Melchior, A. L., & Semelin, B. 2007, A&A, 468, 61
Downes, D., & Solomon, P. M. 1998, ApJ, 507, 615
Elbaz, D., Daddi, E., Le Borgne, D., et al. 2007, A&A, 468, 33
Ellison, S. L., Thorp, M. D., Lin, L., et al. 2020, MNRAS, 493, L39
Ellison, S. L., Lin, L., Thorp, M. D., et al. 2021a, MNRAS, 501, 4777
Ellison, S. L., Wong, T., Sánchez, S. F., et al. 2021b, MNRAS, 505, L46
Fumagalli, M., & Gavazzi, G. 2008, A&A, 490, 571
Fumagalli, M., Krumholz, M. R., Prochaska, J. X., Gavazzi, G., & Boselli, A. 2009, ApJ, 697, 1811
Gao, Y., & Solomon, P. M. 2004, ApJ, 606, 271
García-Burillo, S., Alonso-Herrero, A., Ramos Almeida, C., et al. 2021, A&A, 652, A98
Gavazzi, G., Boselli, A., van Driel, W., & O'Neil, K. 2005, A&A, 429, 439
Gavazzi, G., Boselli, A., Cortese, L., et al. 2006, A&A, 446, 839
Genzel, R., Tacconi, L. J., Gracia-Carpio, J., et al. 2010, MNRAS, 407, 2091
Genzel, R., Tacconi, L. J., Combes, F., et al. 2012, ApJ, 746, 69
Gunn, J. E., Gott, J., & Richard, I. 1972, ApJ, 176, 1
Haines, C. P., Gargiulo, A., La Barbera, F., et al. 2007, MNRAS, 381, 7
Hani, M. H., Hayward, C. C., Orr, M. E., et al. 2020, MNRAS, 493, L87
Haynes, M. P., & Giovanelli, R. 1984, AJ, 89, 758
Huchtmeier, W. K., & Richter, O. G. 1989, A&A, 210, 1
Hughes, A., Meidt, S. E., Schinnerer, E., et al. 2013, ApJ, 779, 44
Isobe, T., Feigelson, E. D., Akritas, M. G., & Babu, G. J. 1990, ApJ, 364, 104
Jáchym, P., Combes, F., Cortese, L., Sun, M., & Kenney, J. D. P. 2014, ApJ, 792, 11
Jáchym, P., Sun, M., Kenney, J. D. P., et al. 2017, ApJ, 839, 114
Jiménez-Donaire, M. J., Bigiel, F., Leroy, A. K., et al. 2019, ApJ, 880, 127
Kennicutt, R. C., Jr., 1983, AJ, 88, 483
Kennicutt, R. C., Jr., 1989, ApJ, 344, 685
Kennicutt, R. C., Jr., 1998, ApJ, 498, 541
Kennicutt, R. C., Jr., Armus, L., Bendo, G., et al. 2003, PASP, 115, 928
Kennicutt, R. C., Jr., Calzetti, D., Walter, F., et al. 2007, ApJ, 671, 333
Klessen, R. S., & Glover, S. C. O. 2016, Saas-Fee Adv. Course, 43, 85
Koopmann, R. A., & Kenney, J. D. P. 2004, ApJ, 613, 866
Kroupa, P., & Weidner, C. 2003, ApJ, 598, 1076
Kuno, N., Sato, N., Nakanishi, H., et al. 2007, PASJ, 59, 117
Lada, C. J., Lombardi, M., & Alves, J. F. 2010, ApJ, 724, 687
Lada, C. J., Forbrich, J., Lombardi, M., & Alves, J. F. 2012, ApJ, 745, 190
Lee, B., & Chung, A. 2018, ApJ, 866, L10
Lee, B., Chung, A., Tonnesen, S., et al. 2017, MNRAS, 466, 1382
Lee, J., Kimm, T., Katz, H., et al. 2020, ApJ, 905, 31
Leroy, A. K., Walter, F., Brinks, E., et al. 2008, AJ, 136, 2782
Leroy, A. K., Walter, F., Bigiel, F., et al. 2009, AJ, 137, 4670
Leroy, A. K., Walter, F., Sandstrom, K., et al. 2013, AJ, 146, 19
Leroy, A. K., Walter, F., Martini, P., et al. 2015, ApJ, 814, 83
Leroy, A. K., Sandstrom, K. M., Lang, D., et al. 2019, ApJS, 244, 24
Leroy, A. K., Hughes, A., Liu, D., et al. 2021, ApJS, 255, 19
Leroy, A. K., Rosolowsky, E., Usero, A., et al. 2022, ApJ, 927, 149
Lin, L., Pan, H.-A., Ellison, S. L., et al. 2019, ApJ, 884, L33
Lizée, T., Vollmer, B., Braine, J., & Nehlig, F. 2021, A&A, 645, A111
Longmore, S. N., Bally, J., Testi, L., et al. 2013, MNRAS, 429, 987
Loni, A., Serra, P., Kleiner, D., et al. 2021, A&A, 648, A31
Lutz, D., Sturm, E., Janssen, A., et al. 2020, A&A, 633, A134

Martin, D. C., Fanson, J., Schiminovich, D., et al. 2005, ApJ, 619, L1
McKee, C. F., & Ostriker, E. C. 2007, ARA&A, 45, 565
Mei, S., Blakeslee, J. P., Côté, P., et al. 2007, ApJ, 655, 144
Meidt, S. E., Leroy, A. K., Querejeta, M., et al. 2021, ApJ, 913, 113
Mok, A., Wilson, C. D., Golding, J., et al. 2016, MNRAS, 456, 4384
Mok, A., Wilson, C. D., Knapen, J. H., et al. 2017, MNRAS, 467, 4282
Moretti, A., Paladino, R., Poggianti, B. M., et al. 2020, ApJ, 889, 9
Morselli, L., Rodighiero, G., Enia, A., et al. 2020, MNRAS, 496, 4606
Moss, C., & Whittle, M. 1993, ApJ, 407, L17
Nehlig, F., Vollmer, B., & Braine, J. 2016, A&A, 587, A108
Orr, M. E., Hayward, C. C., Hopkins, P. F., et al. 2018, MNRAS, 478, 3653
Pan, H.-A., Lin, L., Hsieh, B.-C., et al. 2018, ApJ, 868, 132
Pessa, I., Schinnerer, E., Belfiore, F., et al. 2021, A&A, 650, A134
Pety, J., Schinnerer, E., Leroy, A. K., et al. 2013, ApJ, 779, 43
Querejeta, M., Schinnerer, E., Meidt, S., et al. 2021, A&A, 656, A133
Rahman, N., Bolatto, A. D., Wong, T., et al. 2011, ApJ, 730, 72
Rahman, N., Bolatto, A. D., Xue, R., et al. 2012, ApJ, 745, 183
Repetto, P., Faúndez-Abans, M., Freitas-Lemes, P., Rodrigues, I., & de Oliveira-Abans, M. 2017, MNRAS, 464, 293
Roediger, E., & Brüggen, M. 2007, MNRAS, 380, 1399
Roediger, E., & Brüggen, M. 2008, MNRAS, 388, 465
Rousseeuw, P. J. 1984, J. Am. Stat. Assoc., 79, 871
Ruschel-Dutra, D., Storchi-Bergmann, T., Schnorr-Müller, A., et al. 2021, MNRAS, 507, 74
Saintonge, A., Kauffmann, G., Wang, J., et al. 2011, MNRAS, 415, 61
Saintonge, A., Catinella, B., Cortese, L., et al. 2016, MNRAS, 462, 1749
Sánchez, S. F., Barrera-Ballesteros, J. K., Colombo, D., et al. 2021, MNRAS, 503, 1615
Sandstrom, K. M., Leroy, A. K., Walter, F., et al. 2013, ApJ, 777, 5
Schmidt, M. 1959, ApJ, 129, 243
Schruba, A., Leroy, A. K., Walter, F., Sandstrom, K., & Rosolowsky, E. 2010, ApJ, 722, 1699
Schruba, A., Leroy, A. K., Walter, F., et al. 2011, AJ, 142, 37
Schuster, K. F., Kramer, C., Hitschfeld, M., Garcia-Burillo, S., & Mookerjea, B. 2007, A&A, 461, 143
Shetty, R., Kelly, B. C., & Bigiel, F. 2013, MNRAS, 430, 288
Shetty, R., Kelly, B. C., Rahman, N., et al. 2014, MNRAS, 437, L61
Solanes, J. M., Manrique, A., García-Gómez, C., et al. 2001, ApJ, 548, 97
Sun, J., Leroy, A. K., Schruba, A., et al. 2018, ApJ, 860, 172
Sun, J., Leroy, A. K., Schinnerer, E., et al. 2020, ApJ, 901, L8
Sun, J., Leroy, A. K., Rosolowsky, E., et al. 2022, AJ, 164, 43
Taylor, R., Davies, J. I., Auld, R., Minchin, R. F., & Smith, R. 2013, MNRAS, 428, 459
Thorp, M. D., Ellison, S. L., Pan, H.-A., et al. 2022, MNRAS, 516, 1462
Tonnesen, S., & Bryan, G. L. 2009, ApJ, 694, 789
Usero, A., Leroy, A. K., Walter, F., et al. 2015, AJ, 150, 115
Utomo, D., Bolatto, A. D., Wong, T., et al. 2017, ApJ, 849, 26
Utomo, D., Sun, J., Leroy, A. K., et al. 2018, ApJ, 861, L18
Verdugo, C., Combes, F., Dasyra, K., Salomé, P., & Braine, J. 2015, A&A, 582, A6
Villanueva, V., Bolatto, A. D., Vogel, S., et al. 2022, ApJ, 940, 176
Violino, G., Ellison, S. L., Sargent, M., et al. 2018, MNRAS, 476, 2591
Vollmer, B. 2003, A&A, 398, 525
Vollmer, B., Braine, J., Balkowski, C., Cayatte, V., & Duschl, W. J. 2001, A&A, 374, 824
Vollmer, B., Soida, M., Chung, A., et al. 2008, A&A, 483, 89
Vollmer, B., Soida, M., Braine, J., et al. 2012, A&A, 537, A143
Vollmer, B., Braine, J., Mazzilli-Ciraulo, B., & Schneider, B. 2021, A&A, 647, A138
Vulcani, B., Poggianti, B. M., Finn, R. A., et al. 2010, ApJ, 710, L1
Walter, F., Brinks, E., de Blok, W. J. G., et al. 2008, AJ, 136, 2563
Weiß, A., Walter, F., & Scoville, N. Z. 2005, A&A, 438, 533
Williams, T. G., Gear, W. K., & Smith, M. W. L. 2018, MNRAS, 479, 297
Wilson, C. D. 1995, ApJ, 448, L97
Wilson, C. D., Warren, B. E., Israel, F. P., et al. 2009, ApJ, 693, 1736
Wong, T., & Blitz, L. 2002, ApJ, 569, 157
Wong, T., Blitz, L., & Bosma, A. 2004, ApJ, 605, 183
Wright, E. L., Eisenhardt, P. R. M., Mainzer, A. K., et al. 2010, AJ, 140, 1868
Yoon, H., Chung, A., Smith, R., & Jaffé, Y. L. 2017, ApJ, 838, 81
Zabel, N., Davis, T. A., Smith, M. W. L., et al. 2019, MNRAS, 483, 2251
Zabel, N., Davis, T. A., Sarzi, M., et al. 2020, MNRAS, 496, 2155
Zabel, N., Brown, T., Wilson, C. D., et al. 2022, ApJ, 933, 10
Zschaechner, L. K., Bolatto, A. D., Walter, F., et al. 2018, ApJ, 867, 111

1 Observatorio Astronómico Nacional (IGN), C/Alfonso XII, 3, 28014 Madrid, Spain
e-mail: mdonaire@oan.es
2 Centro de Desarrollos Tecnológicos, Observatorio de Yebes (IGN), 19141 Yebes, Guadalajara, Spain
3 Herzberg Astronomy and Astrophysics Research Centre, National Research Council of Canada, 5071 West Saanich Rd, Victoria, BC V9E 2E7, Canada
4 Department of Physics & Astronomy, McMaster University, 1280 Main St West, Hamilton, Ontario L8S 4M1, Canada
5 Leiden Observatory, Leiden University, PO Box 9513, 2300 RA Leiden, The Netherlands
6 Department of Astronomy, University of Cape Town, Private Bag X3, Rondebosch 7701, South Africa
7 Department of Physics & Astronomy, University of Victoria, Finnerty Road, Victoria, British Columbia V8P 1A1, Canada
8 Department of Astronomy, University of Maryland, College Park, MD 20742, USA
9 Department of Physics & Astronomy, The University of Western Ontario, London, ON N6A 3K7, Canada
10 Institute for Earth and Space Exploration, The University of Western Ontario, London, ON N6A 3K7, Canada
11 Department of Physics, Engineering Physics, and Astronomy, Queen's University, Kingston, ON K7L 3N6, Canada
12 Aix-Marseille Université, CNRS, CNES, LAM, Marseille, France
13 International Centre for Radio Astronomy Research, The University of Western Australia, 35 Stirling Hwy, 6009 Crawley, WA, Australia
14 ARC Centre of Excellence for All Sky Astrophysics in 3 Dimensions (ASTRO 3D), Australia
15 Department of Astronomy, Yonsei University, 50 Yonsei-ro, Seodamun-gu, Seoul 03722, Republic of Korea
16 School of Physics & Astronomy, Cardiff University, Queens Buildings, The Parade, Cardiff CF24 3AA, UK
17 Korea Astronomy and Space Science Institute, 776 Daedeokdae-ro, Yuseong-gu, Daejeon 34055, Republic of Korea
18 Royal Military College of Canada, PO Box 17000, Station Forces, Kingston, ON K7K 7B4, Canada
19 Canadian Institute for Theoretical Astrophysics (CITA), University of Toronto, 60 St George Street, Toronto, ON M5S 3H8, Canada

Appendix A: Additional table and figures

In this section we include a table with the best-fit parameters to the individual molecular KS relations in all the studied VER-TICO galaxies (see Table A.1). In addition to the numerical results, we include the rest of resolved KS relations for the entirety of the VERTICO sample, as a continuation of Fig. 5.

Table A.1. Fits to the individual molecular KS relations ($\Sigma_{\rm SFR} = a\,\Sigma_{\rm mol}^{N}$) in VERTICO.

Galaxy	Index (N)	$\log_{10} A$ (Pearson coeff.) ($\log_{10} M_\odot\,{\rm yr}^{-1}\,{\rm pc}^2$)	$\langle\log_{10}\Sigma_{\rm SFR}/\Sigma_{\rm mol}\rangle$ (p–value)	Scatter (σ) ($\log_{10}\,{\rm yr}^{-1}$)	(dex)
IC3392	0.91 ± 0.04	-3.31 ± 0.09	0.9 (<0.001)	-9.40±0.09	±0.20
NGC4064	1.01 ± 0.05	-3.02 ± 0.10	0.9 (<0.001)	-9.00±0.10	±0.27
NGC4189	0.90 ± 0.02	-2.98 ± 0.05	0.8 (<0.001)	-9.12±0.12	±0.15
NGC4254	0.97 ± 0.01	-3.34 ± 0.04	0.9 (<0.01)	-9.25±0.11	±0.29
NGC4293	1.06 ± 0.04	-2.55 ± 0.09	0.9 (<0.001)	-9.28±0.10	±0.30
NGC4294	0.70 ± 0.05	-2.55 ± 0.04	0.8 (<0.001)	-8.41±0.10	±0.27
NGC4298	0.96 ± 0.01	-3.32 ± 0.03	0.9 (<0.01)	-9.38±0.11	±0.12
NGC4299	1.05 ± 0.10	-2.83 ± 0.31	0.6 (<0.001)	-8.08±0.15	±0.26
NGC4351	1.15 ± 0.06	-2.93 ± 0.09	0.8 (<0.001)	-8.81±0.14	±0.19
NGC4380	0.72 ± 0.03	-3.17 ± 0.03	0.7 (<0.001)	-9.35±0.12	±0.16
NGC4383	1.20 ± 0.03	-3.12 ± 0.21	0.8 (<0.001)	-8.92±0.13	±0.23
NGC4394	0.97 ± 0.06	-3.06 ± 0.11	0.6 (<0.001)	-9.10±0.14	±0.30
NGC4405	0.96 ± 0.04	-3.14 ± 0.12	0.9 (<0.001)	-9.18±0.10	±0.18
NGC4419	0.94 ± 0.02	-3.17 ± 0.06	0.9 (<0.001)	-9.24±0.10	±0.21
NGC4424	1.17 ± 0.06	-3.09 ± 0.20	0.8 (<0.001)	-9.03±0.11	±0.31
NGC4450	0.69 ± 0.05	-3.15 ± 0.03	0.8 (0.001)	-9.32±0.14	±0.25
NGC4457	0.97 ± 0.02	-3.46 ± 0.08	0.9 (<0.001)	-9.57±0.10	±0.20
NGC4501	0.92 ± 0.02	-3.30 ± 0.03	0.9 (<0.01)	-9.41±0.09	±0.18
NGC4532	0.98 ± 0.07	-2.25 ± 0.19	0.7 (<0.001)	-8.33±0.13	±0.34
NGC4535	0.90 ± 0.03	-3.13 ± 0.02	0.8 (<0.01)	-9.24±0.14	±0.28
NGC4536	0.88 ± 0.02	-2.88 ± 0.02	0.9 (<0.01)	-8.90±0.13	±0.25
NGC4548	0.79 ± 0.03	-3.19 ± 0.03	0.8 (<0.001)	-9.32±0.12	±0.21
NGC4561*	–	–	–	–	–
NGC4567	0.70 ± 0.03	-2.78 ± 0.05	0.8 (<0.001)	-9.05±0.11	±0.26
NGC4568	0.84 ± 0.02	-3.12 ± 0.03	0.9 (<0.001)	-9.34±0.10	±0.11
NGC4569	0.82 ± 0.02	-3.32 ± 0.02	0.9 (<0.01)	-9.47±0.12	±0.21
NGC4579	0.83 ± 0.03	-3.21 ± 0.03	0.8 (<0.01)	-9.35±0.12	±0.17
NGC4580	0.82 ± 0.02	-3.18 ± 0.08	0.9 (<0.001)	-9.40±0.10	±0.12
NGC4606	0.93 ± 0.04	-3.24 ± 0.08	0.9 (<0.001)	-9.29±0.11	±0.12
NGC4651	0.79 ± 0.03	-2.80 ± 0.03	0.8 (<0.001)	-9.14±0.11	±0.20
NGC4654	0.81 ± 0.02	-2.93 ± 0.02	0.9 (<0.01)	-9.08±0.12	±0.25
NGC4694	1.40 ± 0.05	-3.31 ± 0.11	0.8 (<0.001)	-9.04±0.13	±0.12
NGC4698	1.04 ± 0.07	-3.09 ± 0.03	0.4 (<0.001)	-9.12±0.17	±0.27
NGC4713	0.82 ± 0.04	-2.51 ± 0.08	0.6 (<0.001)	-8.82±0.14	±0.23
NGC4772*	–	–	–	–	–
NGC4808	0.74 ± 0.03	-2.73 ± 0.02	0.9 (<0.001)	-8.87±0.12	±0.15
Whole sample	0.91 ± 0.04	-3.21 ± 0.12	0.8 (<0.01)	-9.25±0.12	0.23

Notes: Best-fit slope, intercept (referenced to $\Sigma_{\rm mol}$ units of $1\,M_\odot\,{\rm pc}^{-2}$), Pearson correlation coefficient, median value of $\log_{10}\Sigma_{\rm SFR}/\Sigma_{\rm mol}$, and RMS scatter (1-$\sigma$) measured for the resolved KS relation in the individual VERTICO galaxies at 720 pc resolution. (*) Galaxies NGC 4561 and NGC 4772 could not be fitted using a power-law relation. The last row, corresponding to the whole sample, represents the mean values obtained by averaging the previous results for all the individual galaxies. These overall agree with our best-fit results presented in Table 3, within uncertainties.
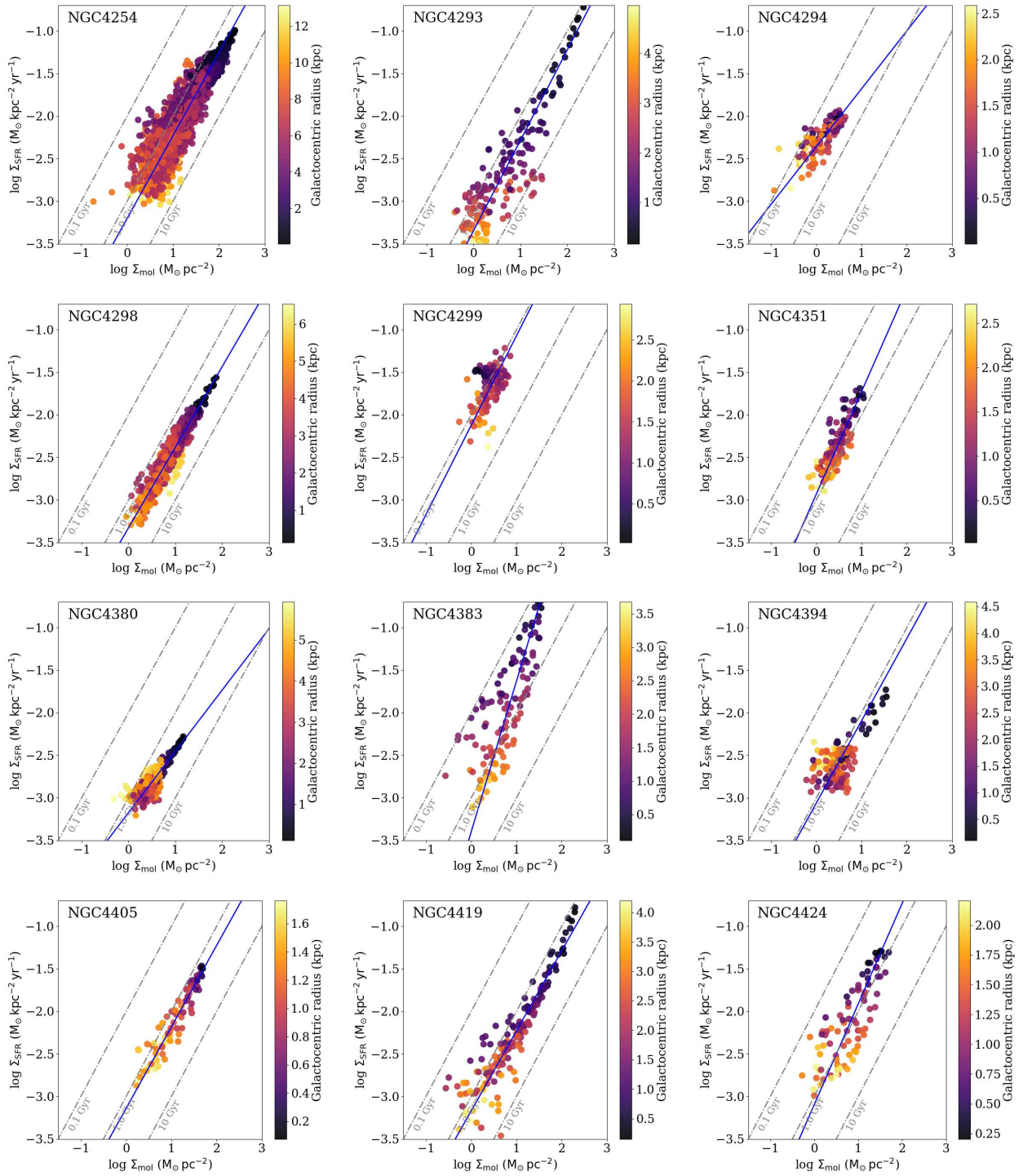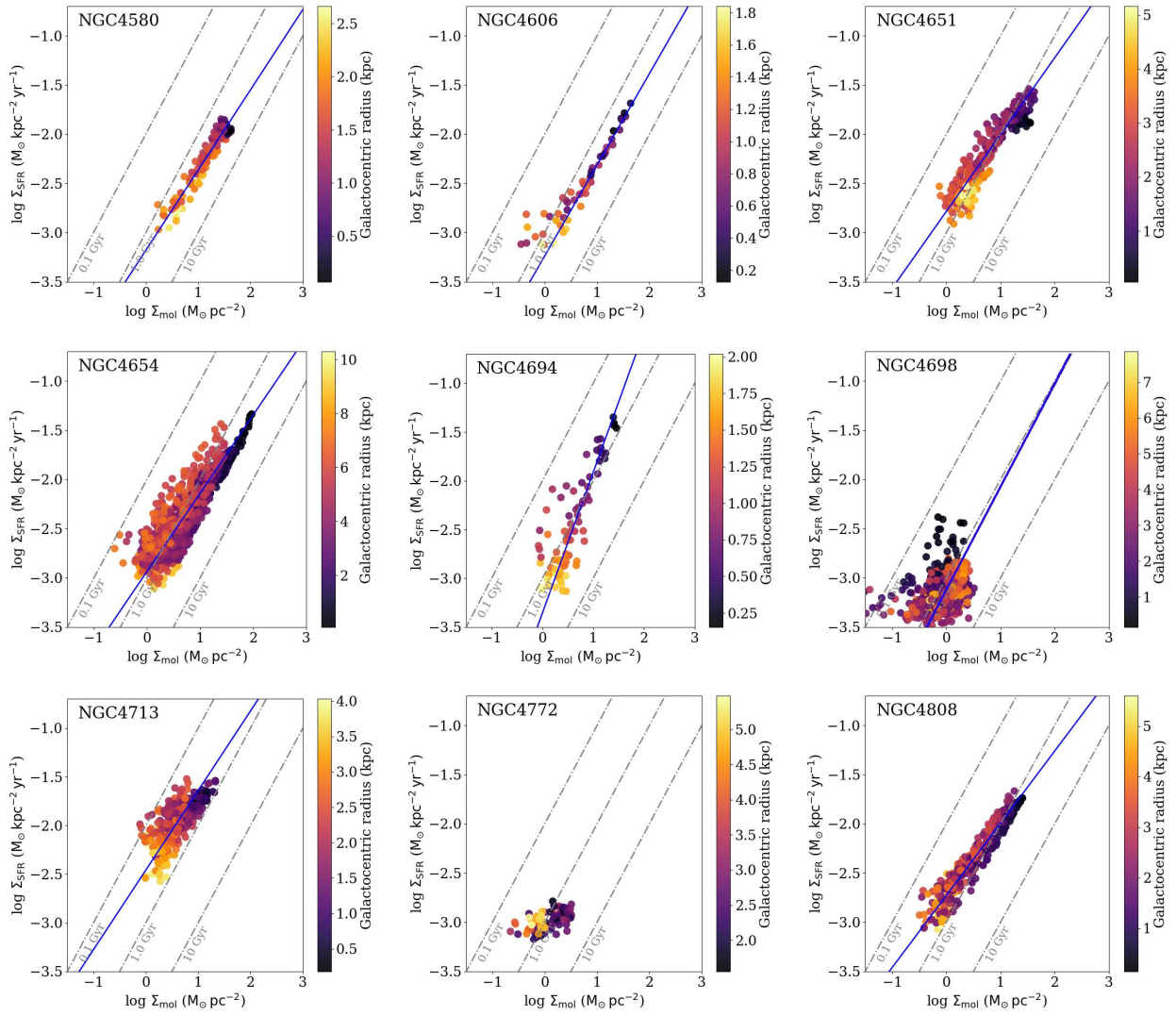
Fig. A.1. The resolved Kennicutt-Schmidt relation for the sub-sample of galaxies in the VERTICO sample. Continuation of Fig. 5.
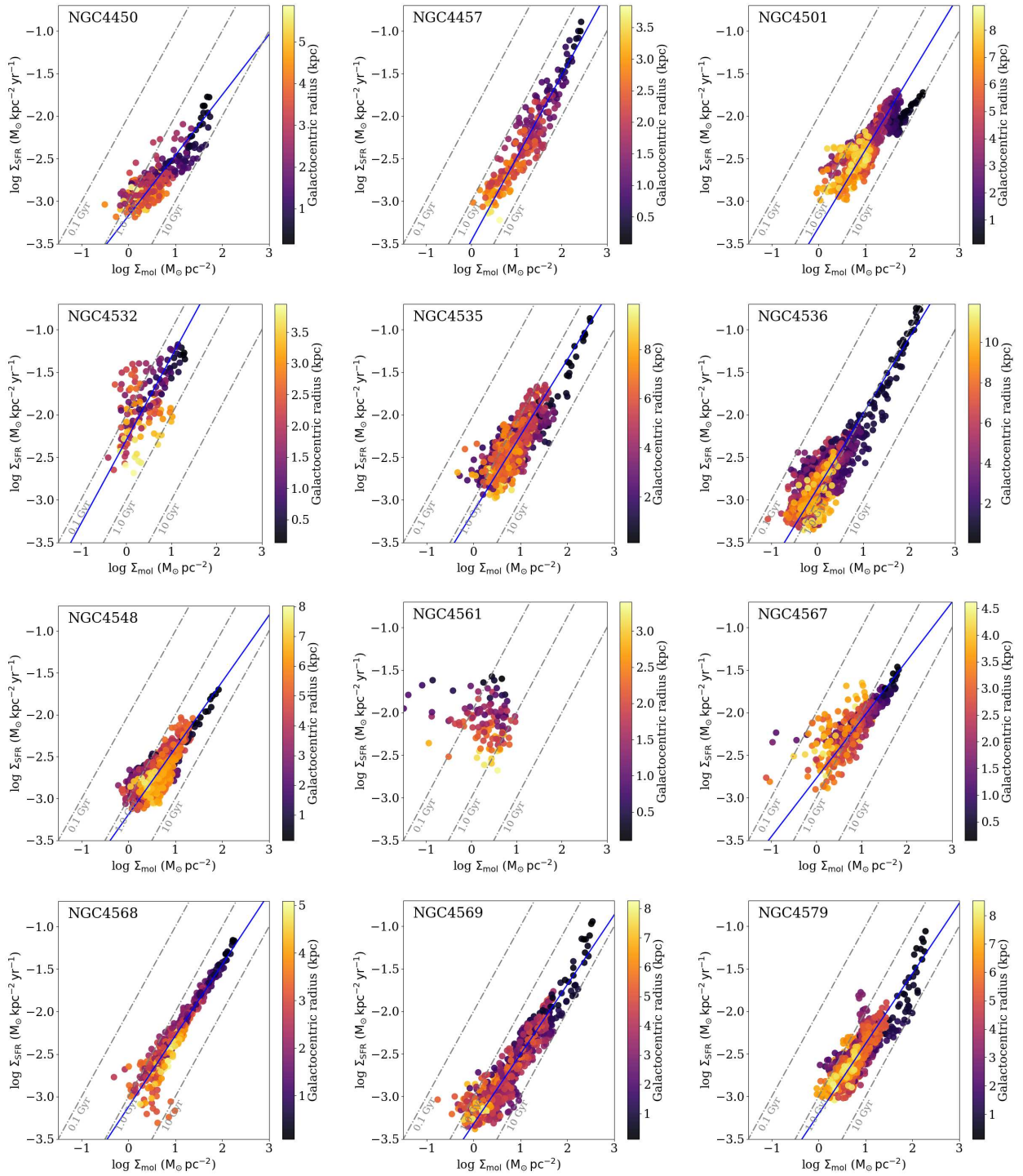
Fig. A.1. continued. Note that we do not provide a robust LTS regression for NGC 4561 since a KS power-law does not appear to be a good fit of the distribution of the data for that galaxy.

Fig. A.1. continued. Note that we do not provide a robust LTS regression for NGC 4772 since a KS power-law does not appear to be a good fit of the distribution of the data for that galaxy.

Appendix B: Observed relations

The full VERTICO survey comprises a total of 51 Virgo Cluster galaxies, which are included in the VIVA survey (Chung et al. 2009). However, a significant fraction of the VERTICO sample is composed of galaxies with highly inclined disks (see Table 1 in Brown et al. 2021, for a complete summary of the basic properties of the full VERTICO sample). In order to minimize the effects of extinction, our sub-sample includes only galaxies with moderate inclinations ($i \leq 80^\circ$).

As described in Sect. 4, the conversion between the observed intensities and the physical quantities, such as molecular gas surface densities, is subject to assumptions and therefore uncertainty. In order to provide an overview of all galaxies belonging to the VERTICO survey, we show our resulting resolved KS relations in Fig. B.1 using direct observables (e.g., $I_{\rm CO}$), without inclination corrections.
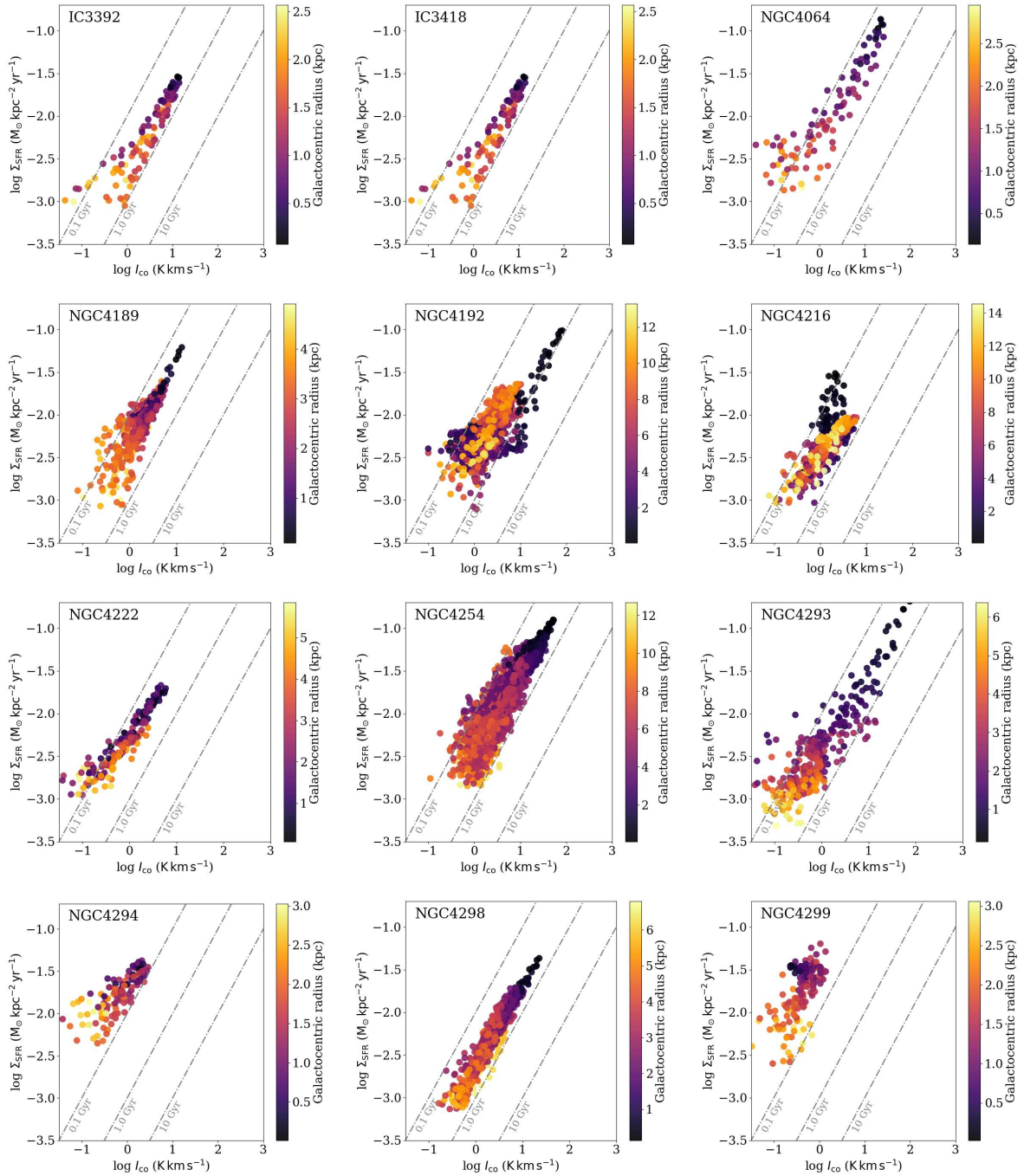
Fig. B.1. The resolved Kennicutt-Schmidt relation for all galaxies in the VERTICO sample, using directly observed CO integrated intensities as a proxy for $\Sigma_{\rm mol}$ as well as the observed $\Sigma_{\rm SFR}$ (e.g., without a correction for cos i). All data points are convolved at a common working resolution of 720 pc. Each data point is color-coded by the distance to the galaxy center. The diagonal dashed, gray lines show constant depletion times of 0.1, 1 and 10 Gyr, respectively.
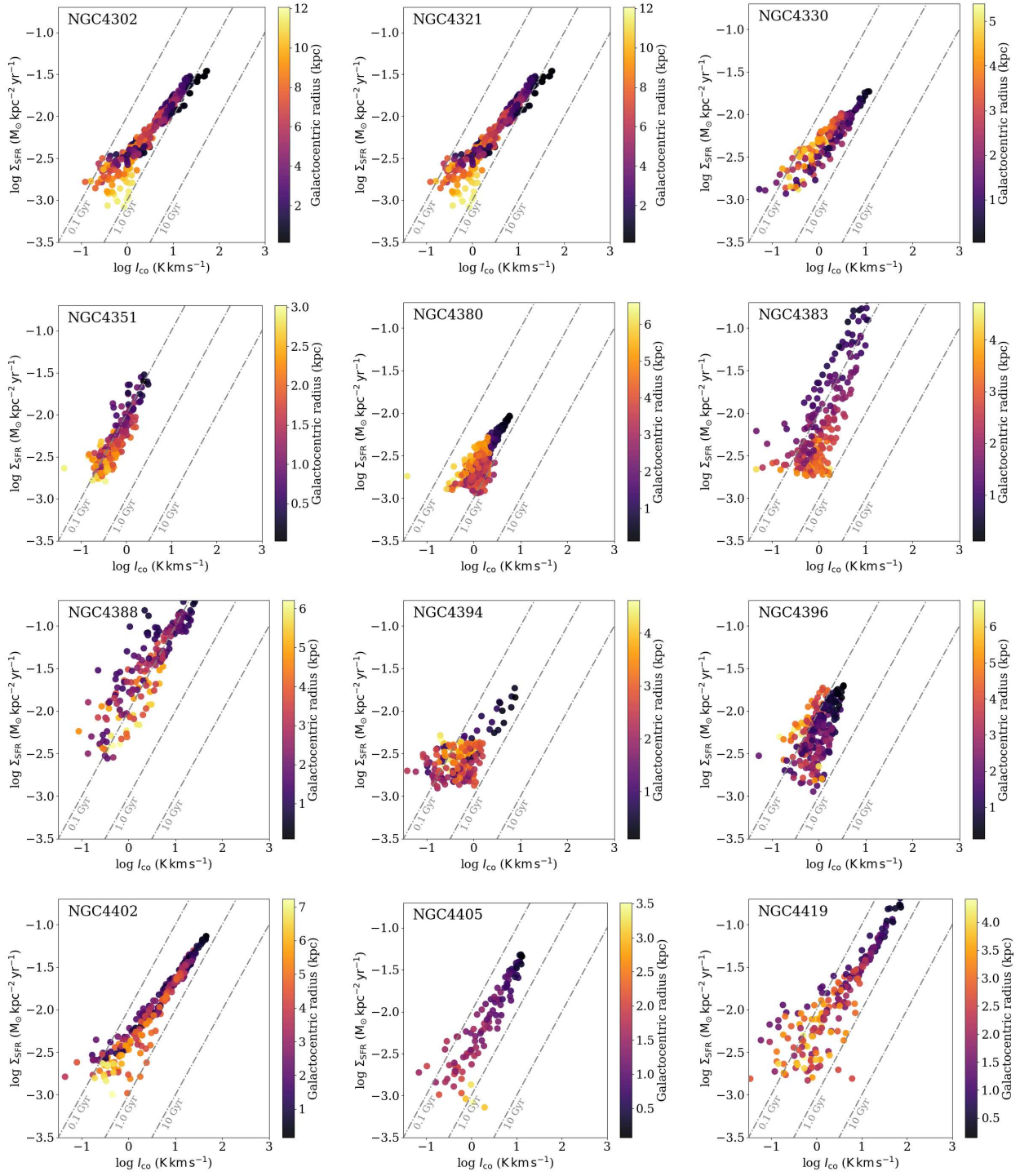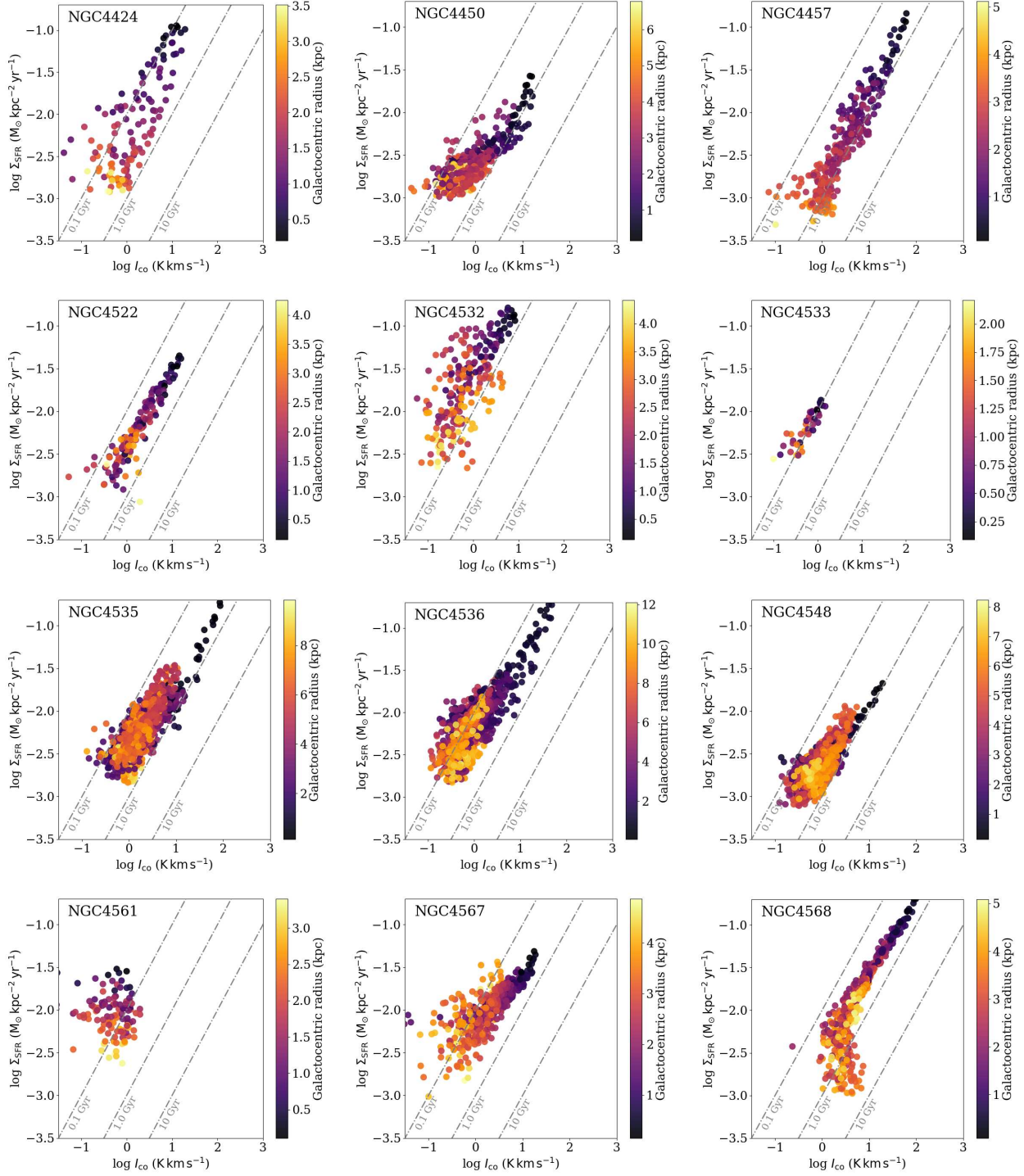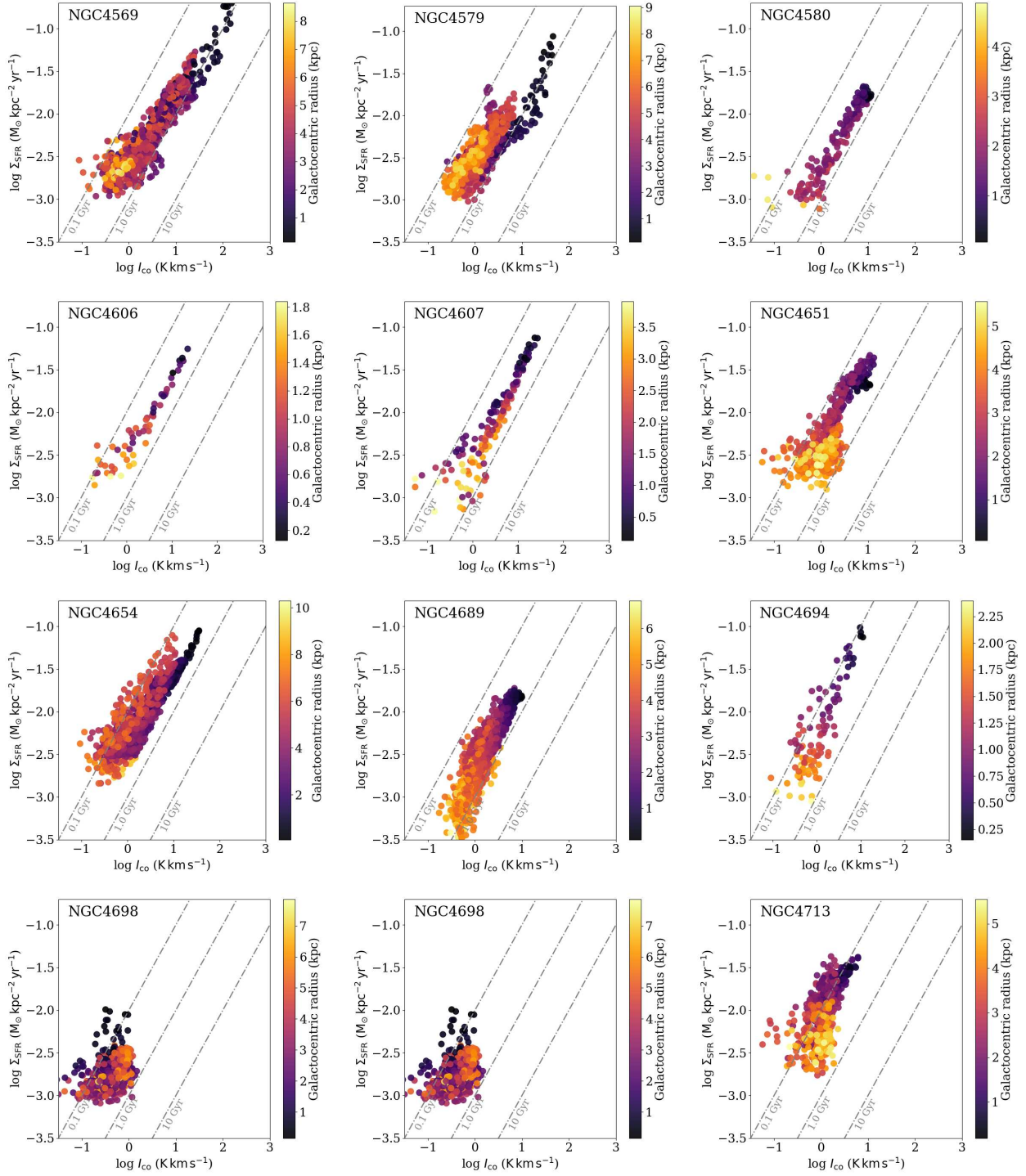
Fig. B.1. continued.

Fig. B.1. continued.

Fig. B.1. continued.

Fig. B.1. continued.